

This item was submitted to [Loughborough's Research Repository](#) by the author.  
Items in Figshare are protected by copyright, with all rights reserved, unless otherwise indicated.

## Delay-induced homoclinic bifurcations in modified gradient bistable systems and their relevance to optimization

PLEASE CITE THE PUBLISHED VERSION

<https://doi.org/10.1063/5.0035959>

PUBLISHER

AIP Publishing

VERSION

VoR (Version of Record)

PUBLISHER STATEMENT

This is an Open Access Article. It is published by AIP under the Creative Commons Attribution 4.0 Unported Licence (CC BY). Full details of this licence are available at: <http://creativecommons.org/licenses/by/4.0/>

LICENCE

CC BY 4.0

REPOSITORY RECORD

Janson, Natalia, and Christopher J. Marsden. 2021. "Delay-induced Homoclinic Bifurcations in Modified Gradient Bistable Systems and Their Relevance to Optimization". Loughborough University.  
<https://hdl.handle.net/2134/18282701.v1>.

# Delay-induced homoclinic bifurcations in modified gradient bistable systems and their relevance to optimization

Cite as: Chaos 31, 093120 (2021); doi: 10.1063/5.0035959

Submitted: 1 November 2020 · Accepted: 26 August 2021 ·

Published Online: 20 September 2021



View Online



Export Citation



CrossMark

Natalia B. Janson<sup>a)</sup>  and Christopher J. Marsden

## AFFILIATIONS

Department of Mathematical Sciences, Loughborough University, Loughborough LE11 3TU, United Kingdom

<sup>a)</sup> Author to whom correspondence should be addressed: [N.B.Janson@lboro.ac.uk](mailto:N.B.Janson@lboro.ac.uk)

## ABSTRACT

Nonlinear dynamical systems with time delay are abundant in applications but are notoriously difficult to analyze and predict because delay-induced effects strongly depend on the form of the nonlinearities involved and on the exact way the delay enters the system. We consider a special class of nonlinear systems with delay obtained by taking a gradient dynamical system with a two-well “potential” function and replacing the argument of the right-hand side function with its delayed version. This choice of the system is motivated by the relative ease of its graphical interpretation and by its relevance to a recent approach to use delay in finding the global minimum of a multi-well function. Here, the simplest type of such systems is explored for which we hypothesize and verify the possibility to qualitatively predict the delay-induced effects, such as a chain of homoclinic bifurcations one by one eliminating local attractors and enabling the phase trajectory to spontaneously visit vicinities of all local minima. The key phenomenon here is delay-induced reorganization of manifolds, which cease to serve as barriers between the local minima after homoclinic bifurcations. Despite the general scenario being quite universal in two-well potentials, the homoclinic bifurcation comes in various versions depending on the fine features of the potential. Our results are a pre-requisite for understanding general highly nonlinear multistable systems with delay. They also reveal the mechanisms behind the possible role of delay in optimization.

© 2021 Author(s). All article content, except where otherwise noted, is licensed under a Creative Commons Attribution (CC BY) license (<http://creativecommons.org/licenses/by/4.0/>). <https://doi.org/10.1063/5.0035959>

Can one predict, without resorting to numerical analysis, the behavior of a nonlinear system with time delay described by a delay-differential equation (DDE) as the delay is gradually increased? Generally not, as it is highly sensitive both to the form of nonlinearities and to how the delay is introduced. Moreover, unlike in ordinary differential equations, their phase space is infinite-dimensional, and it is generally impossible to reverse the time; therefore, nonlinear DDEs represent a challenge both for analytical and numerical treatments. However, here, we construct a special form of highly nonlinear DDEs, in which one can qualitatively predict a sequence of bifurcations as the delay grows. Specifically, we slightly modify the most basic setting for optimization, when the parameter to be optimized decreases—as the negative of the gradient of some multi-well “cost” function (called “potential energy landscape function” in physics problems), by delaying its argument. After overviewsome earlier rigorous results available for simpler DDEs and interpreting them in terms

of the potential function, we use these to predict phenomena in more complex DDEs with two-well potentials, which could be extended to multi-well potentials in the future. We hypothesize and verify some universality in the sequence of global homoclinic bifurcations and also establish how different forms of these bifurcations are realized with different local features of the potential. Delay-induced global bifurcations can be the means to remove the barriers between the local minima of the cost function and thus to allow the phase trajectory to approach all minima, similarly to what occurs in a famous optimization method of simulated annealing thanks to random forces. This effect seems promising for optimization where the delay could replace random forces. Since the barriers are embodied in the manifolds of saddle points or saddle cycles, their reorganization via homoclinic bifurcations is key to understanding how the barriers disappear as the delay grows. We explain rearrangement of manifolds to shed light on this mechanism.

## I. INTRODUCTION

Differential equations with time delay represent a special class of dynamical systems, which are routinely used to model the behavior of both natural systems and artificial devices alongside ordinary differential equations (ODEs). Delay equations have been introduced in the 1940s as models of population dynamics<sup>1,2</sup> and later of other biological phenomena.<sup>3–12</sup> In some models, the delay appears in the term(s) added to the component(s) of the original ODE.<sup>13–15</sup> Other models contain combinations of delayed and non-delayed terms from the outset.<sup>2,16,17</sup>

Delay-differential equations (DDEs) present a considerably greater challenge for the analysis than ODEs because their state is represented by a (vector-) function on an interval rather than by a finite-dimensional vector; hence, the dimension of their phase space is infinitely large. Also, time reversal is generally not permitted, which complicates the detection of unstable objects. Moreover, the effects induced by delay greatly depend on a particular form of the DDE under study and on the exact way the delay is introduced. The latter makes it hardly possible to predict, before resorting to numerical analysis and actually observing the behavior, the dynamics of even a scalar equation with a single delay  $\tau \geq 0$ , i.e., of  $\dot{x} = f(x, x_\tau)$  with  $x, f \in \mathbb{R}$  and  $x_\tau = x(t - \tau)$  for an arbitrary  $f$ .

However, by extending the results from the qualitative theory of ODEs,<sup>18–21</sup> it has been possible to qualitatively predict certain phenomena in special cases. Specifically, some predictions were made for DDEs reducible to the form  $\dot{x} = f(x_\tau) - g(x)$ , often with  $g(x) = \lambda x$  ( $\lambda \in \mathbb{R}$ ),<sup>15,17,22–25</sup> or to an even simpler form  $\dot{x} = f(x_\tau)$  for some special forms of  $f$ .<sup>26</sup> With this, it is usually impossible to give accurate analytical predictions of the behavior of general nonlinear DDEs, and their studies heavily rely on numerical tools. Even more challenging in DDEs is the detection and interpretation of homoclinic and heteroclinic, i.e., global, bifurcations. The reason is that they are based on invariant manifolds, which are usually not confined to a small volume of the phase space (i.e., not localized) and can be one-, two-, many-, or infinite-dimensional. The tools available to date can handle only *unstable* invariant manifolds in DDEs, and examples considered involve one-dimensional<sup>27</sup> and two-dimensional<sup>28,29</sup> manifolds.

Here, we explore a special class of nonlinear DDEs with bistability for which we hypothesize and verify the possibility to predict qualitatively how the behavior changes with the increase of delay. General bistable dynamical systems with delay are popular models in a range of areas, such as optical systems,<sup>30</sup> laser systems,<sup>31</sup> neural networks, atmospheric physics,<sup>32</sup> and ice dynamics;<sup>33</sup> therefore, our work will provide an additional insight into typical bifurcations determining their behavior.

The nonlinear DDE to explore is constructed by modifying a nonlinear ODE with arguably the most predictable behavior, which is the gradient dynamical system of the form

$$\dot{x} = -\nabla V(x), \quad (1)$$

where  $x(t) \in \mathbb{R}$  is the state,  $t$  is the time,  $\dot{x} = \frac{dx}{dt}$ , and  $V(x) : \mathbb{R} \rightarrow \mathbb{R}$  is the potential energy function at least twice continuously differentiable.<sup>34</sup> Also,  $\nabla$  is the gradient operator, which for a scalar  $x$  is equivalent to  $\frac{\partial}{\partial x}$ . This system models the behavior of a particle in a potential energy landscape  $V$  immersed in viscous fluid so that the

particle cannot oscillate. Assuming that  $V$  is a multi-well function with several maxima separating them, the system converges to one of the local minima in a non-oscillatory manner, and the choice of the minimum depends on the initial conditions. System (1) represents the most basic setting for an optimization problem, which in practical applications is posed for  $x(t) \in \mathbb{R}^N$ ,  $V(x) : \mathbb{R}^N \rightarrow \mathbb{R}$  with  $N \geq 1$ , where  $V$  is the multi-well “cost” function, and  $x$  is the vector of parameters in need of optimization.<sup>35,36</sup> Solving this ODE can only deliver a local minimum; therefore, to find the global one, this setting is usually extended to enable the particle to overcome the barriers between the minima. Most popular extensions rely on incorporating random force that makes the particle visit various regions of the landscape, including the vicinity of the global minimum.<sup>37–40</sup>

We delay the argument of the right-hand side of (1) by some amount  $\tau \geq 0$  and thus obtain a DDE to study,

$$\dot{x} = f(x_\tau), \quad f(z) = -\frac{dV(z)}{dz}, \quad (2)$$

where  $x, f, V, z \in \mathbb{R}$ ,  $x_\tau = x(t - \tau)$ . This form of (2) allows us to make some rough qualitative predictions about its solutions based on the knowledge of general bifurcation theory and of general delay-induced effects in dynamical systems. Specifically, in Ref. 41, it was hypothesized and numerically demonstrated that an increase of  $\tau$  could eliminate one by one all local attractors via global homoclinic and possibly heteroclinic bifurcations and give rise to a single large attractor embracing all local minima of  $V$ . Thus, the phase trajectory could be forced to eventually approach all minima of  $V$ , including the global one, regardless of the initial conditions. This means that the delay could roughly mimic the effect from adding large noise to (1), as in global optimization with simulated annealing.<sup>38</sup> However, here, it would be achieved in a fully deterministic manner and through an entirely different mechanism.

Specifically, elimination of local attractors is only possible if their individual basins of attraction cease to be separated by boundaries formed by manifolds of saddle fixed points or of saddle cycles. In the context of optimization, these manifolds serve as the barriers between the minima of  $V$ . After the homoclinic bifurcations, these manifolds do not disappear but reorganize in such a way that they cease being the barriers. Thus, homoclinic bifurcations could effectively break down the barriers between the local minima. This would provide a mechanism, alternative to random noise, for overcoming barriers as required in optimization. With this, understanding of the way the manifolds reorganize as the delay grows would provide the key to understanding if and how optimization by delay could work.

As a starting point and a pre-requisite for understanding the phenomena in delay systems with general multi-well  $V$  depending on one or many variables, here, we focus on system (2) with *two-well* smooth landscape functions  $V$  such that  $V(z) \rightarrow \infty$  as  $|z| \rightarrow \infty$  and  $V, z \in \mathbb{R}$ .

In Sec. II, we overview mathematical theorems related to some simpler delay systems, interpret and illustrate them for the general reader, and put into context of a DDE (2) with energy  $V$ . In Sec. III, we analyze stability of the fixed points of (2) and its relevance to homoclinic bifurcations. In Sec. IV, we combine rigorous theoretical and quantitative results overviewed in Secs. II and III with the powerful apparatus of the qualitative theory of ODEs,<sup>18–21</sup> which has

proved to be successfully applicable to DDEs as well in order to predict, reveal, and explain the rather intricate bifurcation phenomena induced by delay in (2) with a double-well  $V$ . Here, we illustrate these phenomena with specific examples of  $V$  in (2), demonstrate homoclinic bifurcations of various types, and reveal distinctions and universality in the delay-induced behavior of such systems. In Sec. V, we put the delay-induced phenomena in the context of an optimization problem and demonstrate how optimization could work with two local minima if one uses the delay. In Sec. VI, we discuss the results obtained.

## II. DELAY-INDUCED BEHAVIOR IN SIMPLE SYSTEMS

In order to predict some phenomena that might be caused by delay in systems (2) with two- and multi-well landscapes  $V$ , it is important to know about the phenomena occurring in systems with  $V$  having only one well. Note that multi-well functions  $V$  can be obtained by gluing together the segments of single-well  $V$ s and smoothing out all the joints. Thus, bifurcations involving objects localized within a single minimum could be expected in those with more minima, too. This section overviews the results available for functions  $V$  with a single minimum and up to one maximum.

Most theorems formulated for (2) assume that  $\tau = 1$  and  $f$  is amendable;<sup>26,42–50</sup> i.e., the equation reads

$$\frac{dx}{dt} = g(x(t-1)), \quad g(z) = -\frac{dV_1(z)}{dz}. \quad (3)$$

However, introducing  $t = s\tau$  and  $x(t) = y(s)$  reduces (2) to  $\frac{dy}{ds} = \tau f(y(s-1))$ , i.e., to (3) with  $g(z) = \tau f(z)$  and the appropriate change in notations. Thus, the results valid for (3) can be easily adapted to (2) by using the fact that the increase of  $\tau$  in (2) is equivalent to sharpening and deepening the wells of  $V_1$  in (3), as illustrated in Fig. 1.

Note that a typical global bifurcation in the DDEs being considered is associated with the formation of a homoclinic orbit, also called a homoclinic loop, starting and finishing at the same saddle fixed point. For a periodic orbit born from this loop, as the system approaches the bifurcation point, the period tends to become infinitely large. In ODEs, there exists another global bifurcation with the same feature of the periodic orbit involved, called a saddle-node homoclinic bifurcation and otherwise known as SNIPER, which was first described by Andronov in the 1940s (see Sec. 30 of Ref. 51). A SNIPER bifurcation occurs when, as the control parameter changes monotonously, two fixed points (a saddle and a node) move toward each other while staying on the same limit cycle and disappear in a saddle-node bifurcation. After this bifurcation, the whole of the limit cycle becomes the attractor. In the setting we consider, the only control parameter is the time delay  $\tau$ , and in DDEs with constant delays, the number or locations of the fixed points are not affected by the numerical value of the delay. Thus, the increase of the delay alone cannot lead to the movements or the disappearance of the fixed points, and the SNIPER bifurcation cannot occur in the situations we consider in this paper.

The idea of using delay for optimization is inspired by the knowledge of typical behaviors of (3) with relatively simple  $g$ . Although the key relevant theorems are available from highly specialized literature, they have not been previously presented in a form

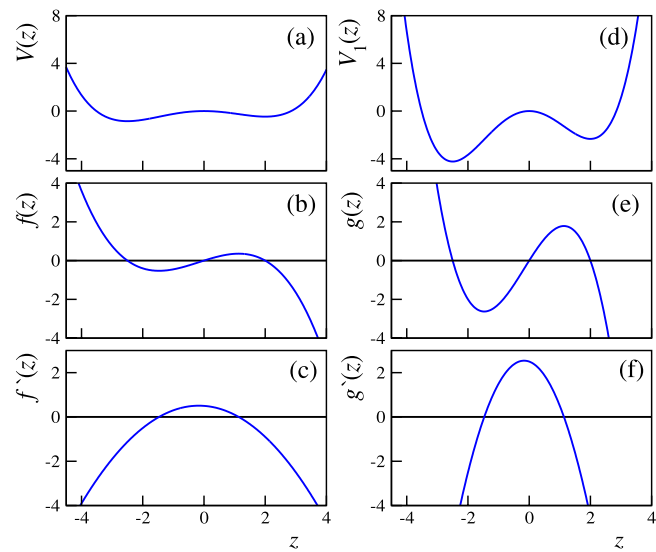


**FIG. 1.** Illustration of the relationship between Eq. (2) with arbitrary  $\tau$  and (3) with  $\tau = 1$  and  $g(z) = \tau f(z)$ . For (2) with  $\tau = 5$ , the left column shows (b)  $f(z) = 0.5z - 0.05z^2 - 0.1z^3$ , (a) the respective landscape  $V(z)$ , and (c)  $f'(z)$ . The right column gives the respective functions for (3), namely, (e)  $g(z) = 5f(z)$ , (d) the landscape  $V_1(z) = 5V(z)$ , and (f)  $g'(z) = 5f'(z)$ .

accessible to a more general reader and not interpreted in the context of the landscape, which we need before explaining how we combine them in order to predict the behavior of (2) with complex-shaped  $V$ . In Subsections II A–II C, three prominent special cases of  $g$  in (3) are considered, namely, monotonically decreasing with a single zero-crossing and making two zero-crossings with a single maximum or a single minimum. We illustrate these cases with specially constructed examples.

### A. Existence of a periodic orbit

In Refs. 42 and 43, Eq. (3) was considered with  $g(z)$  continuously differentiable and monotonically decreasing on some open neighborhood of  $z = 0$ , crossing zero at  $z = 0$ , and in addition satisfying  $zg(z) < 0$  for all  $z \neq 0$ ; i.e.,  $g(z)$  should be strictly positive for negative  $z$  and strictly negative for positive  $z$ . Therefore, the fixed point of (3) is at  $x = 0$ .

In addition,  $g(z)$  should either be bounded from below for all  $z$  [Fig. 2(b)] or satisfy  $|g(z)| \leq A$  if  $|z| \leq A$ , where  $A$  is some positive constant [Fig. 2(d)]. If  $|g'(0)| > \frac{\pi}{2}$ , then (3) has a non-zero periodic solution. In Ref. 45, the stability theorem for this periodic solution is proved. From the viewpoint of the landscape, to enable a periodic solution, the single well of the twice differentiable  $V_1$  should be sufficiently sharp at the bottom [Figs. 2(a) and 2(c)].

Note that the quoted theorems require that  $g(z)$  crosses zero at  $z = 0$ . However, obviously, the same results can be adapted to  $g(z)$  crossing zero at any  $z$  by making an appropriate change of variable. Thus, while the shape of  $g$  contains all the necessary information for the predictions, its localization on the  $z$ -axis is not essential.

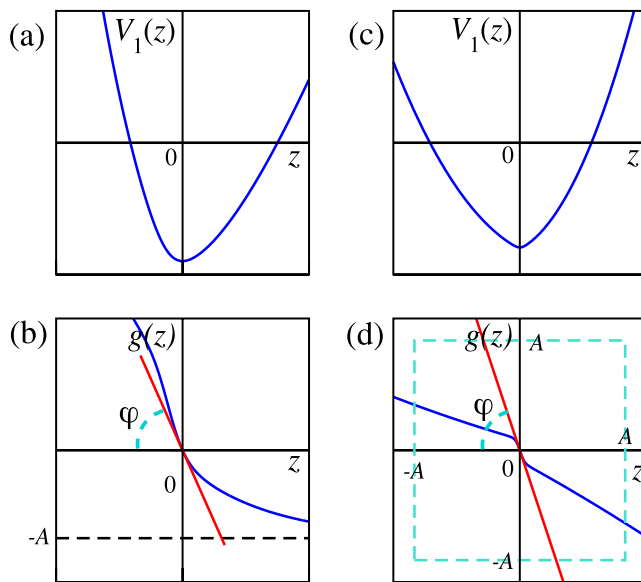


**FIG. 2.** Illustration of the theorems for the existence of periodic solutions in (3). In (b) and (d), blue lines show two functions  $g(z)$  allowing for periodic solutions, and the upper panels (a) and (c) show the respective landscapes. The periodic solution exists if the slope of the tangent line to  $g(z)$  at  $z = 0$  (red line) is  $|g'(0)| = \tan(\varphi) > \frac{\pi}{2}$ . Functions  $g(z)$  are (b)  $g(z) = 8e^{-(z+z^*)/10} - 1 + e^{-(z+z^*)} - 1$  with parameter  $z^* \approx 1.69132$ , such that  $g'(0) \approx -1.72664$ , and (d)  $g(z) = -1 + e^{-10z} - 1 + 0.5 \frac{z}{8} + 1^2 - \frac{2z}{5}$  such that  $g'(0) = -2.9$ .

## B. Existence of a homoclinic orbit to a fixed point

Equation (3) with a non-monotonic  $g$  was studied in Refs. 52 and 53 but rewritten as

$$\frac{dx}{dt} = ah(x(t-1)), \quad a > 0, \quad h(z) = -\frac{dV_2(z)}{dz}. \quad (4)$$

Here,  $h(z)$  is required to cross zero at  $z = 0$  from below to above, and at  $z = -|b|$ ,  $b \in \mathbb{R}$  from above to below. Parameter  $a$  controls the sharpness of the two extrema of  $V_2$ . It has been shown that at certain  $a$ , in (4), there exists a stable periodic orbit around  $x_2 = -|b|$  (red circle in Fig. 3). As  $a$  increases, this orbit grows in size, and, under some additional quantitative conditions on  $h(z)$ , at  $a$  equal to some critical value,  $a^*$  can clash with the saddle fixed point at  $x_1 = 0$  (green circle in Fig. 3) and form a homoclinic loop. At  $a > a^*$ , this orbit no longer exists.

This scenario is illustrated in Fig. 3 for a function  $h(z)$ , which has the required properties on the domain considered [see Fig. 3(a) and caption]. With this  $h$ , Eq. (4) has two relevant fixed points:  $x_2 = -2.5$  (red circle) and  $x_1 = 0$  (green circle) corresponding to the local minimum and maximum of  $V_2$ , respectively [Figs. 3(a) and 3(b)]. At small  $a$ , the point  $x_2$  is stable, but it loses stability at  $a \approx 1.396$  at which  $|ah'(-2.5)| = \frac{\pi}{2}$ . The point  $x_1$  is unstable for any  $a > 0$ . At  $a = 2.24$ , there exists a stable periodic orbit around  $x_2$  shown in Fig. 3(f) in projection on the plane  $(x(t), x(t-1))$ , and the

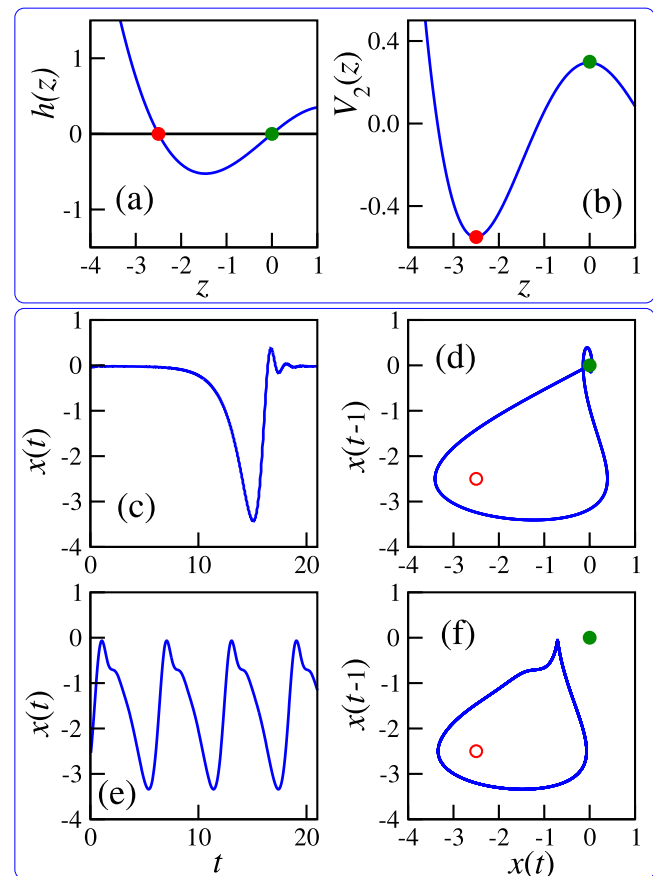


**FIG. 3.** Illustration of the theorem for the occurrence of a homoclinic bifurcation in (4), in which a stable periodic orbit collides with the saddle-focus fixed point to form a homoclinic loop. (a) Function  $h(z) = 0.5z - 0.05z^2 - 0.1z^3$  in a suitable domain  $z \in [-4, 1]$ , which crosses zero at  $z = 0$  and at  $z = -2.5$ , (b) landscape  $V_2$ . Filled circles indicate fixed points: red at the minimum and green at the maximum of  $V_2$ . (c) Homoclinic solution existing at  $a = a^* \approx 2.3765$  and (d) the respective phase portrait. (e) Stable periodic solution and (f) the respective orbit at  $a = 2.24$ . In (d) and (f), empty red circles indicate the unstable (saddle) fixed point  $x = -2.5$  not participating in the homoclinic bifurcation.

respective solution  $x(t)$  is given in (e). At  $a = a^* \approx 2.3765$ , a homoclinic orbit is formed as the periodic orbit collides with  $x_1$ , as shown in (d). In (c), the respective homoclinic solution  $x(t)$  is shown, which departs from  $x = 0$  starting from some time instant in the past and approaches  $x = 0$  as  $t \rightarrow \infty$ .<sup>54</sup>

One can interpret these events in the context of Shilnikov's theorem about the birth of a periodic orbit from the breakdown of the homoclinic loop of a saddle-focus fixed point.<sup>55,56</sup> For  $h(z)$  in Fig. 3(b) for a range of values of  $a > 0$ , the fixed point  $x_1 = 0$  of (4) is a saddle focus with a single real positive eigenvalue  $\lambda_1$ , whereas all of its other eigenvalues are complex-conjugate with negative real parts (see Sec. III). According to Shilnikov's theorem for ODEs and a relevant study of a special form of the DDE (3),<sup>50,52</sup> the breakdown of a homoclinic loop of a saddle-focus gives birth to a periodic orbit if



at the instant of homoclinic bifurcations the loop is “safe.” The latter means that the saddle quantity of this saddle fixed point is negative, i.e.,  $\sigma = \lambda_1 + \text{Re}(\lambda_{2,3}) < 0$ , where  $\lambda_{2,3}$  are eigenvalues with the negative real parts closest to zero.

From this viewpoint, in (4), the homoclinic loop shown in Fig. 3(d) is formed as the parameter  $a$  decreases to its critical value  $a^*$  from above. As  $a$  is further decreased below  $a^*$ , from this homoclinic orbit, a periodic orbit is born [Fig. 3(f)] provided the negativity of  $\sigma$  of the fixed point  $x_1 = 0$ . If  $\sigma > 0$ , then in ODEs, according to Shilnikov, the breakdown of the homoclinic loop should produce chaos rather than periodic behavior.

### C. Existence of chaos from a homoclinic orbit to a saddle cycle

Equation (3) with a relatively simple non-monotonic  $g$  can demonstrate a different sort of a homoclinic bifurcation arising from the tangency of a stable and an unstable manifold of a saddle (hyperbolic) periodic orbit, which can lead to chaos. This global bifurcation was theoretically discovered for ODEs in Refs. 57 and 58 and described in a more accessible manner in Sec. 7.2.1 of Ref. 20. In Refs. 49 and 59, the existence of such chaos has been proved for very specific DDEs for which a solution could be constructed analytically. Also, some general properties of function  $g$  of (3) have been outlined, which should lead to similar behavior. Specifically,  $g(z)$  should cross zero twice: from below to above at smaller  $z$  and from above to below at larger  $z$ . Here, we give an example of a smooth function  $g(z) = ah(z)$  for (3), with  $h(z)$  expressed as

$$h(z) = -\frac{1}{1 + e^{-\frac{z}{2}}} + e^{-\frac{z}{2}} - 2 - e^{-\frac{z}{2}} \quad (5)$$

and illustrated in Fig. 4(a), which for  $a > 0$  possesses the properties given in Refs. 49 and 59. The landscape  $V_2$ , satisfying  $h(z) = -\frac{dV_2(z)}{dz}$ , is given in Fig. 4(b). In this section, we study (4) with  $h$  given by (5), which is equivalent to (3) with  $g(z) = ah(z)$ . We will follow the behavior of (4) and (5) as control parameter  $a$  is varied.

There are two fixed points here:  $x_1 = -1.38629$  (maximum of  $V_2$ , green circle in Fig. 4) and  $x_2 = 0.962424$  (minimum of  $V_2$ , red circle in Fig. 4), which are both saddle for the range of  $a$  illustrated in Figs. 4 and 5.

The saddle cycle, whose manifolds eventually become tangent to each other at the homoclinic bifurcation, is born via the Andronov–Hopf bifurcation from the saddle point  $x_1$  at  $a_{AH} = \frac{1}{h'(z)} \frac{3\pi}{2} \approx 2.8274$  (as explained in Sec. III) and exists for  $a > a_{AH}$ . This saddle cycle (not shown in Fig. 4) is located close to its parent  $x_1$  (green circle).

Like in the example of Sec. II B, here, the homoclinic orbit arises from the tangency of the manifolds of the saddle cycle as the parameter  $a$  decreases to its critical value  $a^* = 3.913$  from above. The manifolds involved in the formation of this orbit are codimension-one (i.e., infinite-dimensional) stable and two-dimensional unstable and cannot be visualized with the numerical tools available to date. However, chaos just born from the manifolds ceasing to be tangent and instead intersecting transversally is visualized with a blue line in Fig. 4(c) at  $a = 3.913$ .

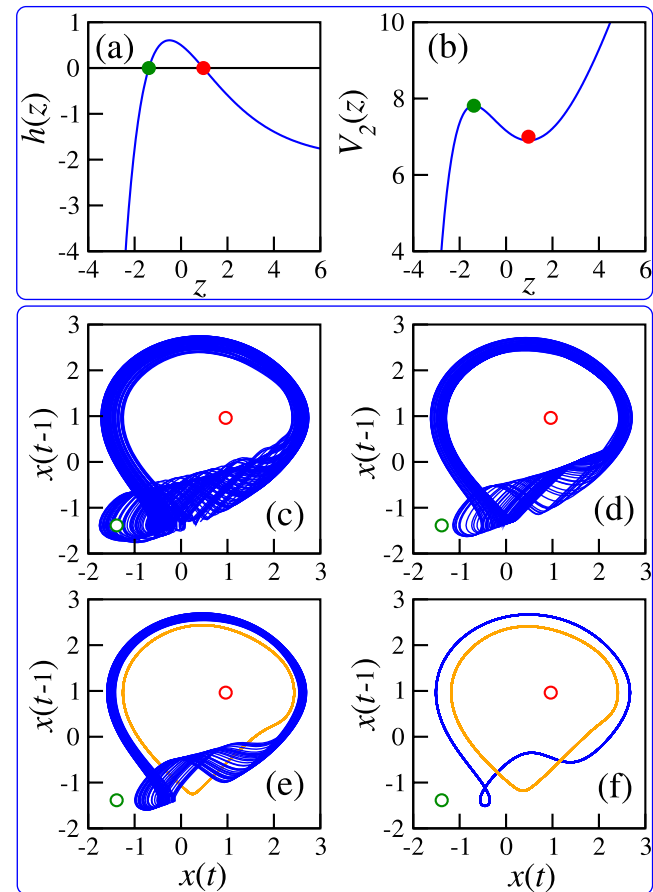


**FIG. 4.** Illustration of the theorem for the occurrence of a homoclinic bifurcation arising from the manifolds of a saddle periodic orbit in (4) and (5) becoming tangent to each other. Compare with the bifurcation diagram in Fig. 5. In (a),  $h(z)$  is shown and in (b) the respective  $V_2(z)$ . (c)–(f) Phase portraits, with parameter  $a$  decreasing from (c) to (f), and empty circles showing fixed points  $x_1$  (green) and  $x_2$  (red), which are both saddle at these values of  $a$ . (c) Chaos from a homoclinic bifurcation at the instant of birth at  $a = 3.913$ , (d) chaos as the only attractor at  $a = 3.85$ , (e) chaos (blue line) coexisting with a stable cycle (orange line) at  $a = 3.8325$ , and (f) two stable cycles of different origins coexisting at  $a = 3.773$ .

Generally, in Figs. 4(c)–4(f), phase portraits are shown for (4) and (5) for several values of  $a$  as  $a$  decreases. Attractors originating from this homoclinic bifurcation are shown by a blue line, and attractors originating from the fixed point  $x_2$  at the landscape minimum (red circle) are shown by an orange line.

The description below can be compared with the bifurcation diagram in Fig. 5. At  $a = 3.913$  [Fig. 4(c)] and  $a = 3.85$  [Fig. 4(d)], chaos born from the homoclinic bifurcation is the only attractor. At  $a \in [3.77, 3.84]$ , two attractors coexist. Figure 4(e) shows that at  $a = 3.8325$ , chaos is born from the homoclinic orbit to the saddle cycle together with the coexistent stable cycle born through the Andronov–Hopf bifurcation from  $x_2$ . In Fig. 4(f) at  $a = 3.773$ , two coexisting stable cycles are given: the one born from homoclinic

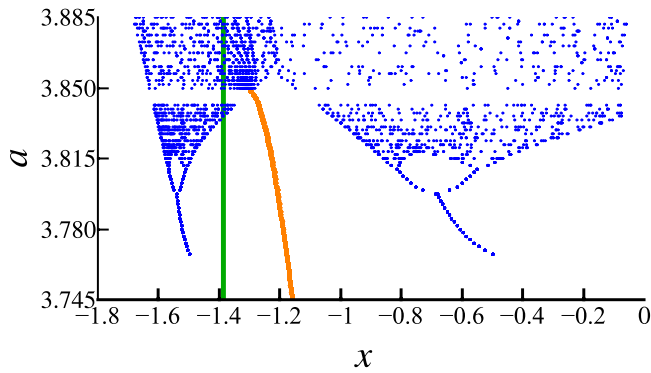


**FIG. 5.** A segment of the bifurcation diagram of (4) with  $h$  given by (5), which for every value of  $a$  shows the local minima of the solution  $x(t)$  (after transients are removed). Blue dots correspond to attractors originating from the homoclinic orbit to the saddle cycle located around the saddle fixed point  $x_1$  at the maximum of  $V_2$  (green line). Orange dots show the attractor originating from the fixed point  $x_2$  at the minimum of  $V_2$ , which is outside the range of  $x$  of this figure. One can clearly see bistability for  $a \in [3.77, 3.85]$ , which means that two attractors of different origins coexist.

chaos in the inverse cascade of period-doubling bifurcations as  $a$  decreases (blue line) and another born from  $x_2$  as  $a$  increases (orange line).

### III. EIGENVALUES OF THE FIXED POINTS

From Sec. II, it becomes apparent that in (2) with a smooth  $V$  having minima and maxima, one should expect an interplay between periodic solutions born from the minima and attractors born from homoclinic bifurcations associated with the maxima directly or indirectly. To predict the behavior of the solution near a minimum or

the one resulting from a homoclinic bifurcation related to a maximum, one needs to know the eigenvalues of the relevant fixed points. In Sec. S-I of the [supplementary material](#), we performed the linear stability analysis of the fixed points of (2) and showed that their eigenvalues  $\lambda_k$  can be expressed in terms of the Lambert function  $W(z)$  with  $z \in \mathbb{R}$  and  $W \in \mathbb{C}$  as

$$\lambda_k = \frac{W_k(J\tau)}{\tau} = \frac{JW_k(z)}{z}, \quad (6)$$

where  $J = f'(x^*)$  and  $x^*$  is the fixed point. Function  $W(z)$  has countably many branches, as illustrated in Fig. S2 of the [supplementary material](#), and  $W_k$  is its  $k$ th branch. Therefore,  $\frac{\lambda_k}{J} = \frac{W_k(z)}{z} = \frac{W_k(J\tau)}{J\tau}$ . Figures 6 and 7 show eigenvalues of the fixed points at the landscape minimum and maximum, respectively (compare with Fig. S2 in the [supplementary material](#)).

Note that at a landscape minimum  $J < 0$ , so with  $\tau \geq 0$ ,  $z = J\tau \leq 0$ . However, in Fig. 6, for convenience, we show  $\frac{\lambda_k}{|J|} = \frac{W_k(-z)}{-z}$  as a function of  $\tilde{z} = |J|\tau \geq 0$ . For  $|J|\tau \in [0, \frac{1}{e}]$ , the leading eigenvalue  $\lambda_1$  (green line) is real and negative, whereas all other eigenvalues are complex with large negative real parts [this is well visible in Figs. 6(b) and 6(d)]. Therefore, the fixed point is effectively a stable node, and the solution converges to it without oscillations. At  $|J|\tau \in [\frac{1}{e}, \frac{\pi}{2}]$ , there is a pair of complex-conjugate leading eigenvalues with negative real parts (red lines in Fig. 6); therefore, in the center manifold of the Andronov–Hopf (AH) bifurcation that occurs at  $|J|\tau = \frac{\pi}{2}$ , the fixed point is a stable focus and the solution converges to it in an oscillatory manner. The boundary between these two subtly different types of behavior is  $\tau = \frac{1}{e}$ , which is highlighted by a vertical green dashed line in Fig. 6, and the respective values of real and imaginary parts of the eigenvalues are highlighted by green filled circles.

In Sec. S-I of the [supplementary material](#), we derive the first condition for the first AH bifurcation of the fixed point  $x^*$  at the

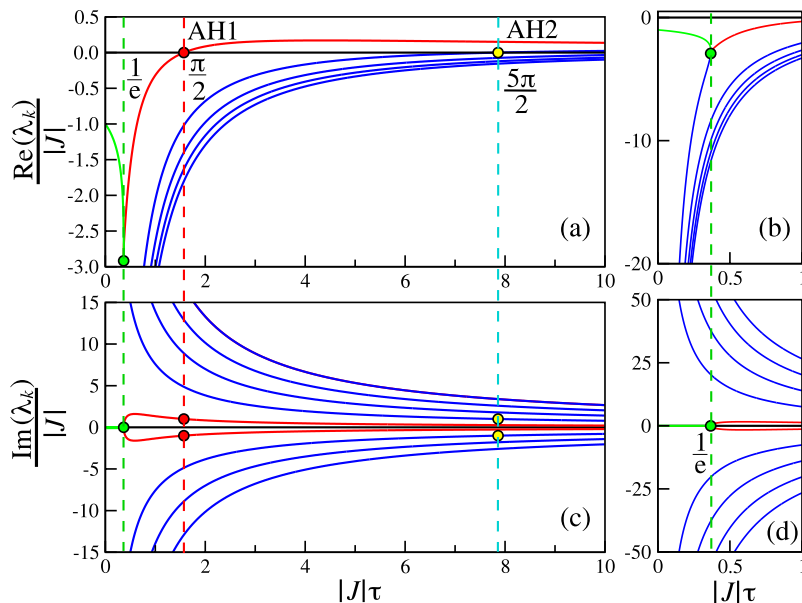


**FIG. 6.** (a) and (b) Real and (c) and (d) imaginary parts of the eigenvalues  $\lambda_k$ , normalized by  $|J|$ , of a fixed point corresponding to a minimum of the landscape  $V(z)$  in (2) as functions of  $|J|\tau$ . In (a) and (b), the leading eigenvalue  $\lambda_1$  (green line) is real for  $|J|\tau \in [0, \frac{1}{e}]$ . At  $|J|\tau > \frac{1}{e}$ , all eigenvalues are complex. At  $|J|\tau = \frac{\pi}{2}$ , the real parts of a pair of leading eigenvalues (red line) cross zero signifying the first Andronov–Hopf (AH) bifurcation marked as AH1 in (a). At  $|J|\tau = \frac{5\pi}{2}$ , the second AH bifurcation takes place, marked as AH2 in (a). Left and right panels show the same functions in different ranges.

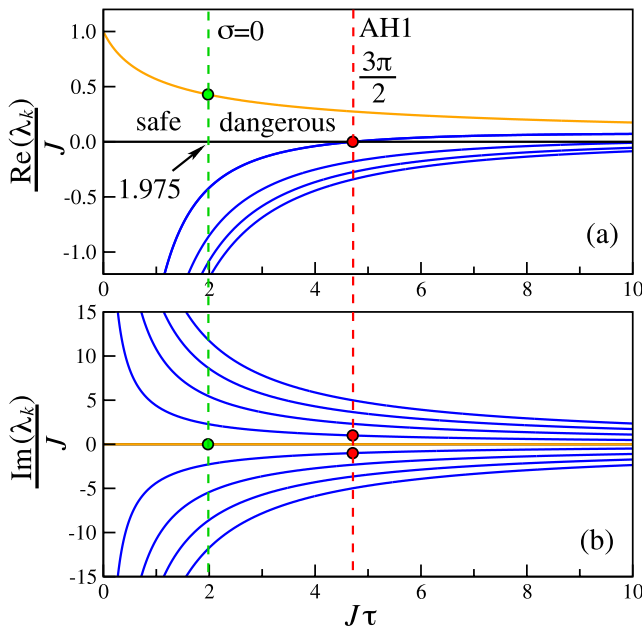


**FIG. 7.** (a) Real and (b) imaginary parts of the eigenvalues  $\lambda_k$ , normalized by  $J$ , of a fixed point corresponding to a maximum of  $V(z)$  in (2) as functions of  $J\tau$ . The leading eigenvalue  $\lambda_1$  (orange line) is real for all  $\tau$ . At  $J\tau \approx 1.975$ , the saddle quantity  $\sigma$  changes sign. At  $J\tau = \frac{3\pi}{2}$ , the first AH bifurcation takes place, marked as AH1.

minimum of  $V$  [Eq. (S11) in the [supplementary material](#)],

$$\tau_{\text{AH1}} = \frac{\pi}{2|J|}, \quad (7)$$

and verify the second condition [Eq. (S18) in the [supplementary material](#)]. Equation (7) is consistent with the predictions for the existence of a periodic solution in (3) for a special form of  $g(z)$  as discussed in Sec. II A. However, this result is more general and applies to a smooth  $f$  of any shape. Thus, Eq. (7) allows one to determine the value of  $\tau$  at which it is possible for the stable cycle to be born from the fixed point at the landscape minimum. The first AH bifurcation, AH1, is highlighted by the vertical red dashed line in Fig. 6, and the respective values of real and imaginary parts of the eigenvalues are highlighted by red filled circles. At  $\tau_{\text{AH2}} = \frac{5\pi}{2|J|}$ , the second AH bifurcation occurs, as a result of which a saddle cycle could be born around the minimum. The second AH bifurcation, AH2, is highlighted with a vertical dashed cyan line in Fig. 6, and the respective values of real and imaginary parts of the eigenvalues are highlighted by yellow filled circles.

For a fixed point at the maximum of  $V$ ,  $J > 0$ , and Fig. 7 shows  $\frac{\lambda_k}{J} = \frac{W_k(J\tau)}{J}$  as a function of  $J\tau \geq 0$ . One can see that, as also confirmed by the analysis in Sec. S-I of the [supplementary material](#), at any  $\tau \geq 0$ , there is one real positive eigenvalue  $\lambda_1$  (orange line); therefore, this fixed point is always unstable for non-negative  $\tau$ . However, it is important to appreciate that for  $J\tau \in [0, \frac{3\pi}{2}]$ , this point is a saddle-focus with a one-dimensional unstable manifold and an infinite-dimensional (codimension-one) stable manifold. As

shown in (S19) of the [supplementary material](#), at  $J\tau = \frac{3\pi}{2}$ , or at

$$\tau_{\text{AH1}} = \frac{3\pi}{2J}, \quad (8)$$

the first AH bifurcation occurs, which is highlighted by a vertical red dashed line in Fig. 7, and the respective values of eigenvalues are marked by red filled circles. For visualization purposes, for  $J\tau \in [0, \frac{3\pi}{2}]$ , we can mentally replace the stable infinite-dimensional manifold of the saddle-focus with a two-dimensional center manifold of its first AH bifurcation. In this approximation, the given fixed point would represent a saddle-focus with a one-dimensional unstable manifold and a two-dimensional stable manifold, as explained in more detail in Sec. IV. If there is a well of  $V$  nearby, the stable and unstable manifolds can form a homoclinic loop at some  $\tau$  from inside  $[0, \frac{3\pi}{2J}]$ . With this, Shilnikov's theorem for ODEs<sup>55,56</sup> verified for a special form of (3)<sup>50,52</sup> predicts that for a safe loop with  $\sigma < 0$  (see Sec. II B for the definition of  $\sigma$  and Shilnikov's theorem), which exists for  $J\tau \in [0, 1.975]$ , the homoclinic loop breaks down to form a stable periodic orbit. If the loop is dangerous with  $\sigma > 0$ , the resultant regime should be chaotic at least in ODEs,<sup>55,56</sup> although to the best of our knowledge, this was not verified for DDEs.

Note that at  $\tau_{\text{AH1}}$ , a saddle periodic orbit is born from the saddle point at the maximum, which is an intersection of a stable and an unstable manifold. At larger  $\tau$ , the manifolds of this saddle orbit can form a loop, whose breakdown can give birth to chaos, as discussed in Sec. II C.

#### IV. DELAY-INDUCED BEHAVIOR IN SYSTEMS WITH TWO-WELL POTENTIALS

A two-well landscape function  $V$  in (2) can be constructed by gluing together segments of single-well landscapes considered in Sec. II and smoothing out the joints. This observation leads us to suggest that the phenomena discussed in Sec. II should also occur in different parts of the phase space of (2) with a two-well  $V$ . However, a two-well function has a different quality as compared to a single-well one; therefore, it is reasonable to also expect new phenomena not covered in Sec. II.

It follows from Sec. II that homoclinic bifurcations play a central role in DDEs (3) with non-monotonic  $g(z)$  of even very simple shapes and result in the disappearance of local attractors when  $g$  becomes sufficiently steep. The nature of the homoclinic bifurcations depends on the fine local features of  $g$ , but their occurrence seems inevitable as the steepness parameter grows. For (2), an equivalent of the steepness parameter is  $\tau$ ; therefore, the homoclinic bifurcations are expected to occur as  $\tau$  grows.

In this section, we verify our prediction that homoclinic bifurcations should occur in systems (2) with two-well potentials  $V$ . We reveal that the occurrence of the particular forms of such bifurcations depends on the individual features of the potential wells and a hump, such as the depth, width, and sharpness, as well as on the relationships between them.

We illustrate our findings using two subtly different examples of  $V$ , which lead to homoclinic bifurcations of different kinds. For this purpose, we construct the functions  $V$  in such a way that by adjusting parameters, we could control their local features. The first example is considered in this section and the second one in Sec. S-II



of the [supplementary material](#). However, our additional studies with the forms of  $V$  specified in Sec. S-III of the [supplementary material](#), which are not reported here due to the lack of space, suggest the generality and reproducibility of the phenomena discovered for the landscapes with the same qualitative features.

In relation to optimization, a particularly important phenomenon at large delays is the disappearance of localized attractors and the existence of the global chaos, which enables the phase trajectory to spontaneously visit the neighborhoods of all local minima. This effect is similar to the action of random noise on (1) within simulated annealing<sup>38</sup> and superficially might seem quite simple. However, the mechanisms leading to global chaos are quite intricate and involve considerable rearrangements of manifolds belonging to saddle fixed points or to saddle cycles while the system undergoes a chain of homoclinic bifurcations. It is thanks to these global bifurcations that the barriers separating the vicinities of local minima disappear. Therefore, understanding reorganization of manifolds is crucial for understanding why and how the delay could help in optimization. In this section, we explain what happens to manifolds by applying the knowledge about homoclinic bifurcations available from the qualitative theory of ODEs and verify its predictions with numerical simulations of (2).

### A. Model

Here, we consider bifurcations in (2) with a double-well  $V$  and the respective  $f = -V'$  specified as follows:

$$\begin{aligned} V(x) &= -\frac{1}{2}e^{-2(x-1)^2} - e^{-0.5(x+3)^2} + 0.01(x+1)^4 - 0.88, \\ f(x) &= -2e^{-2(x-1)^2}(x-1) - e^{-0.5(x+3)^2}(x+3) \\ &\quad - 0.04(x+1)^3. \end{aligned} \quad (9)$$

The functions  $V(x)$ ,  $f(x)$ , and  $J(x) = f'(x)$  are shown in Fig. 8(a) by blue, red, and green lines, respectively. The constant  $(-0.88)$  was added in  $V$  in order to make the graphs better distinguishable from each other. The upper part of Table I summarizes the local features of  $V$  in (9), including the positions of two minima  $x_{1,2}^{\min}$  and one maximum  $x^{\max}$ , their depths  $V_{1,2}^{\min}$  and  $V^{\max}$ , Jacobians  $J_{1,2}^{\min}$  and  $J^{\max}$ , and the points of the first AH bifurcations  $\tau_{1,2}^{\text{AH1}}$  and  $\tau^{\text{AH1}}$ . In Fig. 8(a), red circles indicate the positions of  $x_{1,2}^{\min}$ , which are stable fixed points of (2) at  $\tau = 0$ , and the green circle shows the fixed point at the landscape maximum  $x^{\max}$ , which is unstable at  $\tau = 0$  and saddle at any  $\tau > 0$ .

In the context of optimization illustrated in Sec. V, we remark that in this  $V$ , the minimum  $x_1^{\min}$  is the lowest of the two, and the respective well is the broadest and has the flattest bottom.

### B. Overview of bifurcations

The single control parameter in (2) and (9) is  $\tau$ , and the bifurcation diagram is shown in Fig. 8(b). Specifically, vertical red lines show the locations of fixed points  $x_1^{\min}$  and  $x_2^{\min}$  for the range of  $\tau$  inside which they remain stable. At  $\tau = \tau_{1,2}^{\text{AH1}}$  where the lines stop (values are given in Table I), AH bifurcations occur in agreement with (7). The green vertical line shows  $x^{\max}$  in the whole range of  $\tau$  considered.

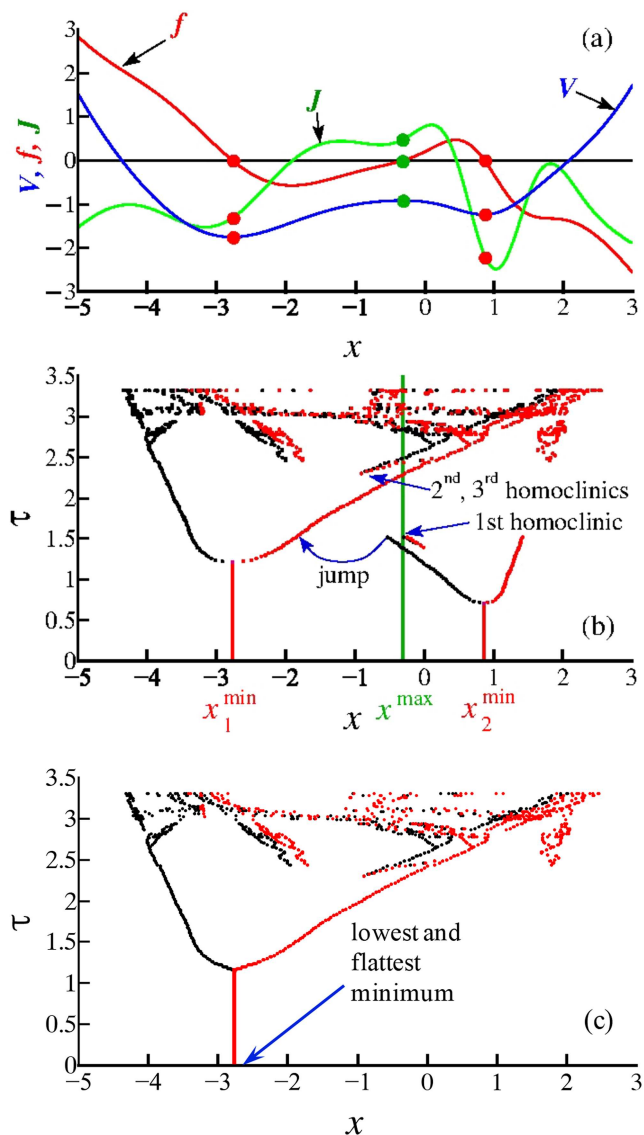


**FIG. 8.** (a) Functions  $V(x)$  (blue line),  $f(x)$  (red line), and  $J(x) = f'(x)$  (green line) specified by (9). Red/green circles show positions of fixed points at the minima/maxima of  $V$ . (b) Bifurcation diagram of (2) and (9). Local minima/maxima of attractors are shown by black/red dots. Fixed points at the minima of  $V$  are shown by red vertical lines for  $\tau$  at which they are stable, and the saddle-focus at the maximum of  $V$  is shown by a green vertical line. As  $\tau$  varies, in this system, only safe homoclinic loops are formed by the manifolds of the saddle-focus fixed point  $x^{\max}$ . (c) Demonstration of optimization. Local maxima (red dots) and minima (black dots) of solutions to (2) and (9) are shown, which are obtained as  $\tau$  slowly decreases from 3.3 to zero. The solution spontaneously settles down at the lowest, flattest, and broadest minimum  $x_1^{\min}$ . Compare with (a) and (b).

For oscillatory attractors, red/black dots indicate local maxima/minima of  $x(t)$ , which constitute the projections of the Poincaré sections defined as  $\dot{x} = 0$ ,  $\ddot{x} < 0/\ddot{x} > 0$ , respectively. Note that this diagram is different from the classical bifurcation diagrams, such as

**TABLE I.** Features of the minima and a maximum of the potential  $V$  specified by (9) and the points of homoclinic bifurcations in (2) and (9) as  $\tau$  grows. This table provides the locations of the minima  $x_{1,2}^{\min}$  and the maximum  $x^{\max}$ , their depths  $V_{1,2}^{\min}$  and  $V^{\max}$ , Jacobians  $J_{1,2}^{\min}$  and  $J^{\max}$ , and the points of the first AH bifurcations  $\tau_{1,2}^{\text{AH1}}$  and  $\tau^{\text{AH1}}$ . For  $x^{\max}$ ,  $\tau^{\sigma}$  is the value of  $\tau$  at which its saddle quantity switches from negative to positive. All homoclinic bifurcations here are homoclinic loops of the saddle-focus fixed point at  $x^{\max}$ , which are safe since all values of  $\tau J^{\max}$  are below 1.975. All numerical values in the table are given approximately.

Features of the potential $V$ in (9)		
$x_1^{\min} = -2.771\ 68$	$x_2^{\min} = 0.864\ 388$	$x^{\max} = -0.308\ 654$
$V_1^{\min} = -1.7557$	$V_2^{\min} = -1.2417$	$V^{\max} = -0.9207$
$J_1^{\min} = -1.300\ 15$	$J_2^{\min} = -2.195\ 11$	$J^{\max} = 0.490\ 368$
$\tau_1^{\text{AH1}} = 1.208$	$\tau_2^{\text{AH1}} = 0.7155$	$\tau^{\text{AH1}} = 9.61$
flattest, broadest, lowest		$\tau^{\sigma} = 4.0276$
Homoclinic bifurcation points in (2) and (9)		
1st homoclinic (safe small loop of $x^{\max}$ ): $\tau = 1.53$ , $\tau J^{\max} = 0.75$		
2nd homoclinic (safe large loop of $x^{\max}$ ): $\tau = 2.4307$ , $\tau J^{\max} = 1.19$		
3rd homoclinic (safe small loop of $x^{\max}$ ): $\tau = 2.4499$ , $\tau J^{\max} = 1.201$		

the one in Fig. 5, which usually show only one kind of the attractor extrema. We show both kinds of the extrema because we need to illustrate how the sizes of the limit cycles born from AH bifurcations grow with  $\tau$  and how the attractors approach the saddle point  $x^{\max}$ . This representation allows us to register homoclinic bifurcations from the abrupt changes in the locations and/or amplitudes of the numerically found attractors under very small changes in  $\tau$ .

Altogether, there are three homoclinic bifurcations, as indicated in Fig. 8(b) and in Table I. Whereas the 1st homoclinic bifurcation can be easily detected from Fig. 8(b), the details of the 2nd and 3rd ones are hard to see in this scale. To demonstrate these convincingly, an enlarged segment of the bifurcation diagram in the relevant area is provided in Fig. 9.

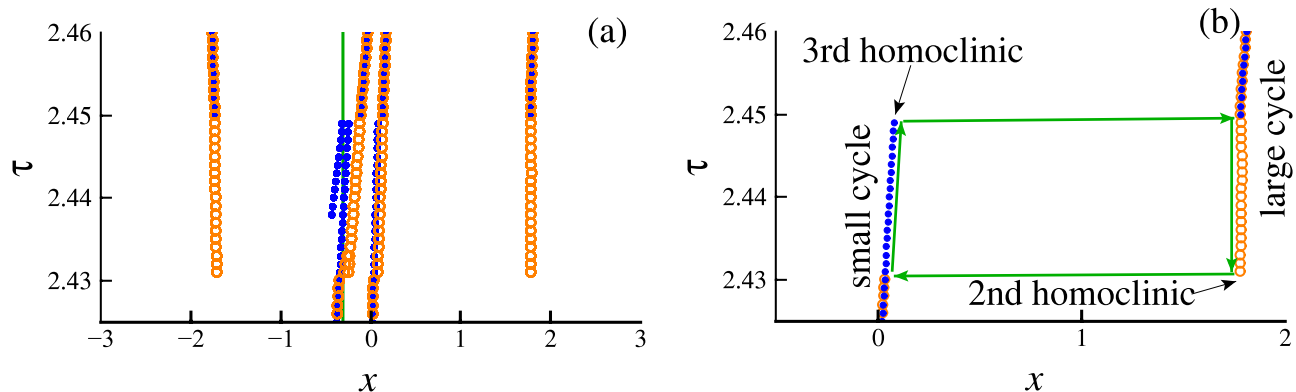


**FIG. 9.** (a) Segment of the bifurcation diagram in Fig. 8(b) illustrating 2nd and 3rd homoclinic bifurcations, bistability, and hysteresis in (2) and (9). Circles show all maxima of the attractors (limit cycles): as  $\tau$  increases (blue filled) and as  $\tau$  decreases (orange empty). The vertical green line shows  $x^{\max}$ . (b) The *largest* maxima of the attractors is shown to demonstrate hysteresis more clearly: as  $\tau$  increases (blue filled) and as  $\tau$  decreases (orange empty). A hysteresis loop is marked by green arrows. The relevant small and large cycles are shown in Fig. 10(h) by red and turquoise lines, respectively.

Below, we will state our predictions about the details of delay-induced homoclinic bifurcations, which can be made on the basis of rigorous results overviewed in Secs. II C and III. These will be verified and illustrated with phase portraits in Fig. 10, which complement the bifurcation diagram in Fig. 8(b).

The point  $x^{\max}$  is of a saddle-focus type for  $\tau > 0$ . Within the range of  $\tau$  shown in Fig. 8(b), it has a single real positive eigenvalue  $\lambda_1$  corresponding to a one-dimensional unstable manifold and countably many complex-conjugate eigenvalues with negative real parts corresponding to a stable manifold of codimension one. In other words,  $x^{\max}$  does not undergo an AH bifurcation and does not give birth to a saddle cycle. Therefore, we should not be expecting the situation described in Sec. II C, and all homoclinic bifurcations here must consist of the closure of the manifolds of  $x^{\max}$  itself to form a one-dimensional loop, following the scenario of Sec. II B.

Based on Sec. II B, we can predict that the formation from the loop of a new attractor, which would be localized near  $x_{1,2}^{\min}$ , would occur as  $\tau$  passes the bifurcation point from above to below, i.e., *decreases*. If we consider the sequence of events as  $\tau$  is increased, then the localized attractor existing at  $\tau$  below the bifurcation point would approach  $x^{\max}$ , collide with it while the manifolds close at the bifurcation, and cease to exist for  $\tau$  above the bifurcation.

The predicted scenario is confirmed for the 1st and 3rd homoclinic bifurcations illustrated with phase portraits in Figs. 10(a)–10(d) and 10(i)–10(l), respectively. As a result of these bifurcations, the localized attractors disappear one after another. However, the 2nd homoclinic bifurcation does not follow from Sec. II B and is of a different type. Specifically, as  $\tau$  grows, this bifurcation produces a large limit cycle embracing all fixed points [see Figs. 10(e)–10(h)].

Figures 9(a) and 9(b) show that in a small range  $\tau \in [2.4307, 2.4499]$ , i.e., between the 2nd and 3rd homoclinics, the system demonstrates bistability as the large cycle coexists with the smaller one around  $x_{1,2}^{\min}$  until the latter disappears via the 3rd homoclinic. There is also a hysteresis meaning that by slowly and continuously increasing and decreasing  $\tau$ , one observes different attractors.

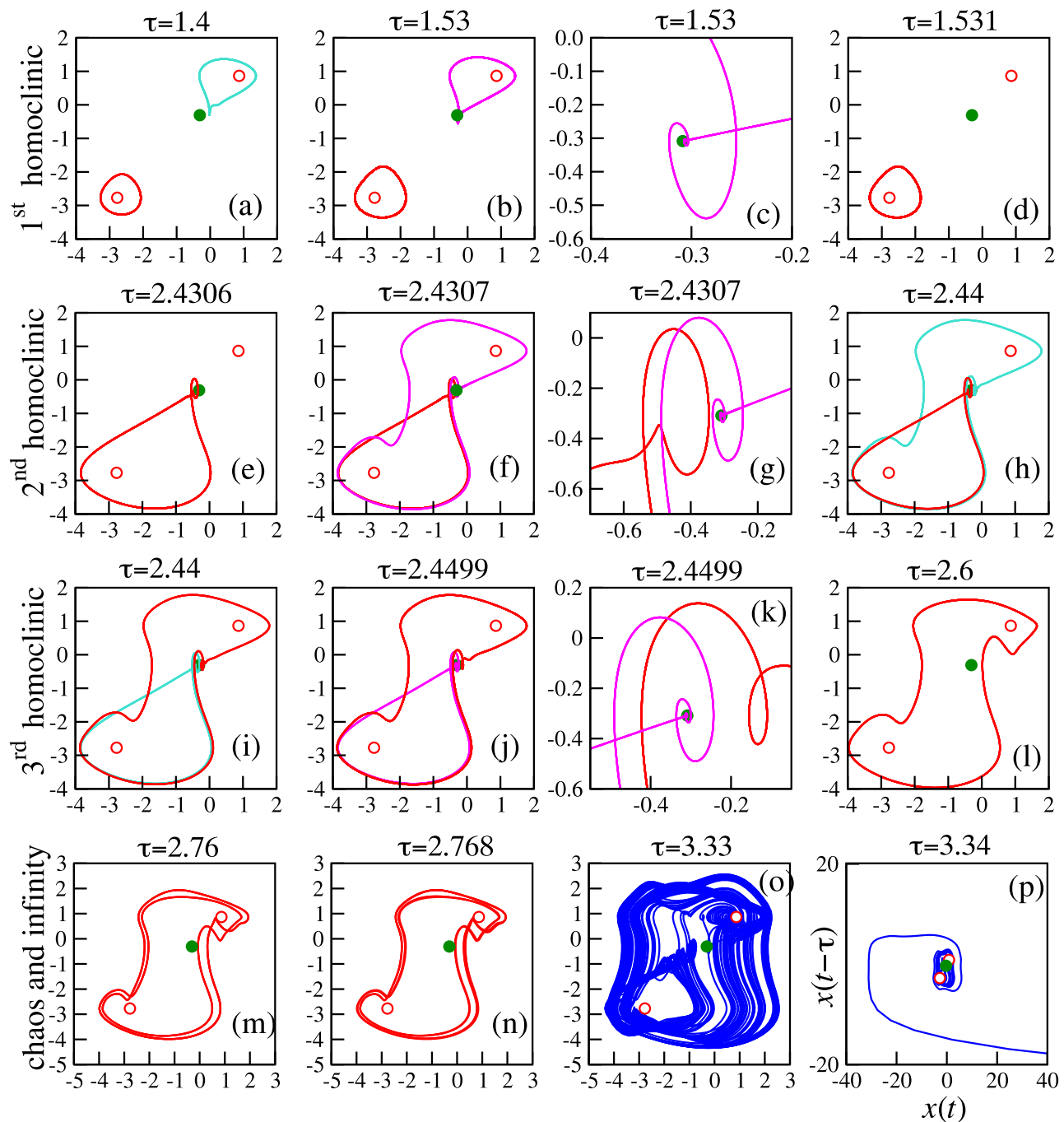


**FIG. 10.** Phase portraits of (2) and (9) illustrating bifurcation diagrams in Figs. 8 and 9 with  $\tau$  given in panels. Notations are fixed points  $x_{1,2}^{\min}$  (red circles) and  $x^{\max}$  (green circle), filled/empty circles indicate points below/above AH bifurcations; attractors (red and turquoise lines), and homoclinic loops (magenta line). 1<sup>st</sup> row: (a) Before, (b) and (c) at, and (d) after the 1st homoclinic bifurcation. Small cycle around  $x_2^{\min}$  [turquoise line in (a)] collides with  $x^{\max}$  to form a homoclinic loop [magenta line in (b) and (c)] around  $x_2^{\min}$  and disappears (d). 2<sup>nd</sup> row: (e) Before, (f) and (g) at, and (h) after the 2nd homoclinic bifurcation. (e) Small cycle around  $x_1^{\min}$  is the only attractor, (f) and (g) homoclinic loop of  $x^{\max}$ , (h) large cycle born from a homoclinic loop (turquoise line) coexisting with a small cycle around  $x_1^{\min}$  (red line). 3<sup>rd</sup> row: (i) Before, (j) and (k) at, and (l) after the 3rd homoclinic bifurcation. (i) Large (red line) and small (turquoise line) cycles coexist, (j) and (k) cycle around  $x_1^{\min}$  collides with  $x^{\max}$  and forms a homoclinic loop, and (l) large cycle is the only attractor. 4<sup>th</sup> row: (m) period-2 cycle, (n) period-4 cycle, (o) chaos embracing all fixed points at large  $\tau$ , and (p) trajectory goes to infinity at even larger  $\tau$ .

Specifically, Fig. 9(a) shows *all* local maxima of an attractor as  $\tau$  increases (blue filled circles) and as  $\tau$  decreases (orange empty circles). The lack of the full coincidence between the blue and orange circles is an evidence of hysteresis. Also, a hysteresis loop is shown by green arrows in (b) where only the largest maxima of the attractors are given for clarity.

To predict whether the attractors colliding with  $x^{\max}$  at homoclinic bifurcations are limit cycles or chaotic attractors, we need to establish whether the respective loops are safe or dangerous, respectively, based on the sign of the saddle quantity  $\sigma$ , as explained in Secs. II B and III. Specifically, as mentioned in Sec. III, for DDEs, the quantity  $\sigma$  is negative and the loop is safe when  $\tau J^{\max} < 1.975$ , implying the collision with a stable limit cycle. For all three homoclinic bifurcations, Table I gives the values of  $\tau$  together with  $\tau J^{\max}$ , the latter being smaller than 1.975. Therefore, we expect safe loops in all three homoclinic bifurcations.

Phase portraits in Figs. 10(a)–10(l) comply with this prediction and show limit cycles being destroyed by [(a)–(d) and (i)–(l)], or born from [(e)–(h)], the homoclinic bifurcations as  $\tau$  increases.

### C. Role of manifolds in homoclinic bifurcations

The key components of homoclinic bifurcations are invariant manifolds, and it is their reconfiguration that induces most drastic changes in the observed system behavior associated with the death or birth of attractors. Here, at  $\tau > 0$ , different basins of attraction are separated by the *stable* manifolds of the saddle-focus  $x^{\max}$ . Therefore, in the context of optimization, these stable manifolds form the barriers between the vicinities of the local minima of  $V$ . Therefore, to understand if and how local attractors in (2) and (9) can disappear as  $\tau$  grows, one needs to understand how these manifolds are reconfigured.

Whereas the attractors of nonlinear DDEs can be detected numerically with relative ease, revealing and plotting *manifolds* of such systems is a challenge. Some methods to visualize two-dimensional manifolds in nonlinear ODEs have been introduced in Refs. 60 and 61 and *unstable* manifolds in DDEs in Refs. 29 and 62. However, the phase space of a DDE is infinite-dimensional, implying that the stable manifold of  $x^{\max}$  has dimension infinity and is thus highly challenging to detect and to depict. Moreover, revealing a stable manifold in an ODE would require reversing time, which is generally not possible in DDEs.<sup>63</sup> With this, to the best of our knowledge, there are no techniques available to date to numerically obtain stable manifolds of DDEs.

While being unable to reveal by direct numerical visualizations how the manifolds reorganize in DDEs, we can still explain this at a qualitative level by extending the results from the qualitative theory of ODEs,<sup>21</sup> which are supported by numerical visualizations of such reorganizations during homoclinic bifurcations of a saddle-node<sup>64</sup> and a saddle-focus<sup>65</sup> in a three-dimensional system of ODEs. Our explanations and predictions are illustrated with Figs. 11–13, which can be compared with the phase portraits in Fig. 10. Although the phase portraits can supply only a highly limited information, their agreement with the predicted effects would provide a reasonably acceptable level of verification for these.

The manifolds of a saddle-focus near a homoclinic loop are quite intricate in shape. To make our explanation clearer, we start

from considering some fictional two- and three-dimensional systems, which we assume to demonstrate similar homoclinic bifurcations occurring to a saddle-node, whose manifolds are simpler than those of a saddle-focus [see Figs. 11(a)–11(j) and 12].

Next, in order to schematically illustrate homoclinic bifurcations in a DDE, we will proceed by analogy with a center manifold reduction in ODEs.<sup>66</sup> Specifically, we will assume that the dynamics on the infinite-dimensional (codimension-one) stable manifold of the saddle-focus  $x^{\max}$  of (2) and (9) can be approximated by the dynamics on the two-dimensional manifold associated with the leading pair of complex-conjugate eigenvalues of this point. Thus, we will explain reorganization of manifolds of a saddle-focus in (2) and (9) by sketching manifolds, fixed points, limit cycles, and homoclinic loops in a three-dimensional phase space in Figs. 11(k)–11(o) and Fig. 13.

### D. First homoclinic bifurcation

In Fig. 11, panels (a)–(e) show snapshots of manifolds, fixed points, and limit cycles at consecutive values of a certain control parameter of a fictional two-dimensional system undergoing the simplest orientable homoclinic bifurcation, which is roughly similar to the 1st homoclinic bifurcation in (2) and (9). Here, the saddle-node (green circle) is an equivalent of  $x^{\max}$ . Dashed lines show manifolds affected by the homoclinic bifurcation, and solid lines show manifolds unaffected by it. Other notations are given in the figure caption.

An equivalent sequence of events in a three-dimensional system is illustrated in Figs. 11(f)–11(j). The only difference from Figs. 11(a)–11(e) is that the stable manifold of the saddle-node is two-dimensional here. Depiction of all manifolds in a 3D space helps to make a transition from a homoclinic loop of a saddle-node to that of a saddle-focus because the latter can exist only in spaces of dimension three and higher.

Next, Figs. 11(k)–11(o) schematically illustrate manifolds of the saddle-focus and other objects in the phase space of (2) and (9): (k)–(m) before, (n) at, and (o) after the 1st homoclinic bifurcation. The notations are specified in the figure caption.

The saddle-focus [green filled circle in Figs. 11(k)–11(o)] is an intersection of the two-dimensional stable manifold (cyan surface, a segment is shown) and the one-dimensional unstable manifold (blue line) associated with the only real and positive eigenvalue of this point. The stable manifold is the boundary between the attractor basins of two attractors (red filled circles or red lines).

Below, we compare Figs. 11(k)–11(o) with the bifurcation diagram in Fig. 8(b) and with the phase portraits in Figs. 10(a)–10(d). As  $\tau$  grows from zero, the following events precede the 1st homoclinic bifurcation. At  $\tau \in [0, 0.7155]$ , there are two coexisting stable fixed points [Fig. 11(k)] at  $x_1^{\min}/x_2^{\min}$  below/above the stable manifold of  $x^{\max}$  [compare with Fig. 8(b)].

At  $\tau \approx 0.7155$ ,  $x_2^{\min}$  undergoes AH bifurcations, and the stable cycle is born from it. The situation just above this bifurcation is illustrated in Fig. 11(l), where the red line above the stable manifold shows a newly born cycle. At  $\tau \approx 1.208$ ,  $x_1^{\min}$  undergoes AH bifurcations, and the stable cycle is born from it, which for a slightly larger  $\tau$  is given by the red line below the cyan surface in Fig. 11(m) [compare with Fig. 10(a)]. With this, the first limit cycle [upper red

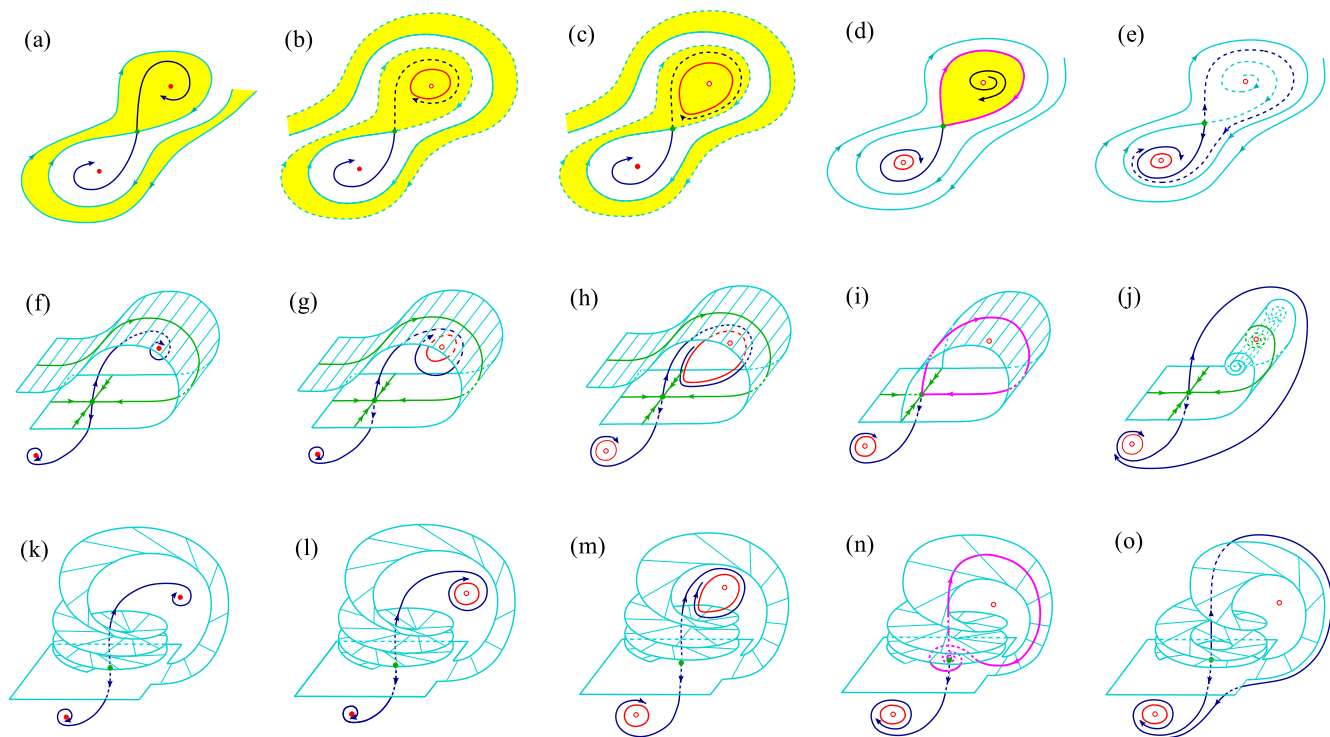


**FIG. 11.** Schematic illustration of the 1st homoclinic bifurcation in (2) and (9) eliminating the first localized attractor. (a)–(j) Illustrations of a homoclinic bifurcation of a saddle-node in some fictional systems of dimensions (a)–(e) two and (f)–(j) three as some control parameter monotonously changes from (a) to (e) and from (f) to (j), respectively. (k)–(o) Illustration of a homoclinic bifurcation of a saddle-focus  $x^{\max}$  in (2) and (9), as the value of  $\tau$  increases from (k) to (o). Filled red circles show stable fixed points, and empty red circles show fixed points above AH bifurcations, a green filled circle shows (a)–(j) a saddle-node and (k)–(o) a saddle-focus, and red lines show stable cycles. In (d), (i), and (n), the magenta line shows the homoclinic loop. In (a)–(e), yellow and white shades show basins of attraction of two different attractors, and dashed lines in (b), (c), and (e) show manifolds involved in homoclinic bifurcations. Cyan/blue lines show stable/unstable manifolds of the saddle-node. In (f)–(j), cyan surfaces show stable manifolds and blue lines show unstable manifolds of the relevant saddle point. In (f)–(j), a green line with double arrows is a strong stable manifold of the saddle-node, which is contained in its stable 2D manifold, and green lines with single arrows are trajectories on the stable 2D manifold, which approach the saddle point along its eigenvector corresponding to the larger of two negative eigenvalues.

line in 11(m) and turquoise in 10(a)] has grown in size and stretched toward the saddle focus.

At  $\tau \approx 1.53$ , the 1st homoclinic bifurcation occurs; specifically, the limit cycle around  $x_2^{\min}$  collides with  $x^{\max}$ , and the unstable manifold of the latter “sticks” to its own stable manifold and forms a homoclinic loop [magenta lines in Fig. 11(n) and in Figs. 10(b) and 10(c)]. This bifurcation is identical to the one illustrated in Fig. 3 as one goes from (f) to (d).

As  $\tau$  increases slightly beyond the value of the 1st homoclinic of 1.53, the local attractor on the right side of  $x^{\max}$ , i.e., near  $x_2^{\min}$ , ceases to exist. The system has a single attractor left, which is the limit cycle localized near  $x_1^{\min}$  [compare red lines in Figs. 10(d) and 11(o)]. If at  $\tau$  just above 1.53 the initial conditions are set on or near the just disappeared local attractor around  $x_2^{\min}$ , the phase trajectory swiftly leaves this region and converges to the limit cycle around  $x_1^{\min}$  in what might feel like a “jump” as indicated in Fig. 8(b).

Unlike in the homoclinic bifurcation of a saddle-node illustrated in Figs. 11(a)–11(j), the shape of the stable manifold of the saddle-focus is quite intricate. Specifically, close to the homoclinic

bifurcation, part of the stable manifold of  $x^{\max}$  returns to the vicinity of  $x^{\max}$  from above and takes the shape of an open helicoid with a finite number of turns [see the upper part of Figs. 11(k)–11(m)], with turns coming closer to each other as they come closer to the saddle-focus, as numerically demonstrated for a 3-dimensional dynamical system in Ref. 65.

At the instant of homoclinic bifurcation (n), the helicoid becomes closed and develops an infinite number of turns such that the distance between the consecutive turns becomes smaller as the turns come closer to  $x^{\max}$ . At the same instant, the unstable manifold “sticks” to this closed helicoid and forms a loop (n). After the homoclinic bifurcation, the helicoid opens and possesses a finite number of turns again (o). As a result of homoclinic bifurcations, the one-dimensional unstable manifold (blue line) “permeates” through the stable one (cyan surface), and the latter no longer separates basins of attraction. A more detailed discussion of the attractor basins is given in Sec. IV E.

Figures 11(k)–11(o) schematically show only a small portion of the stable manifold near the homoclinic loop. However, in reality,



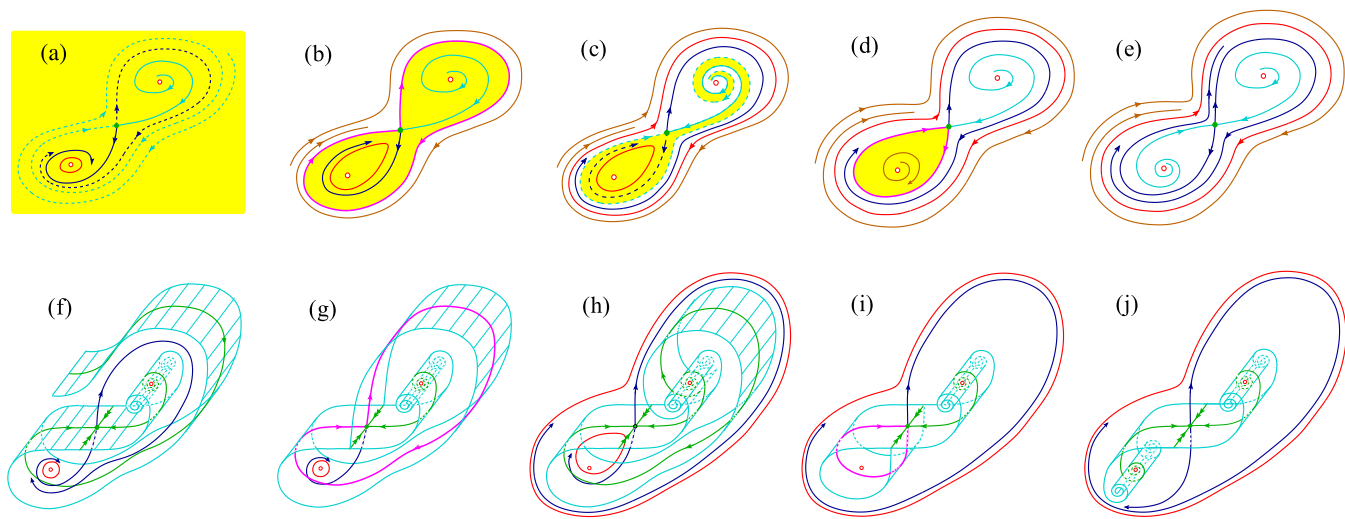


**FIG. 12.** Schematic illustration of homoclinic bifurcations in some fictional (a)–(e) two-dimensional and (f)–(j) three-dimensional systems, respectively, with a saddle-node, which are similar to the 2nd and 3rd homoclinic bifurcations of the saddle-focus in (2) and (9) with safe loops forming as  $\tau$  is increased from 2.425 to 2.46 as shown in Fig. 9. Notations are as in Fig. 11, and in addition in (b)–(e), the brown line shows a typical phase trajectory. Away from the saddle-node, the stable manifold (cyan line or surface) behaves in the same manner qualitatively as with a saddle-focus [compare (f) and (g) with Fig. 13]. In (b) and (g), the 2nd homoclinic bifurcation is illustrated, in which a large safe loop (magenta line) is formed by the manifolds of the saddle-node [compare with Figs. 10(f) and 13(d)]. This bifurcation leads to the birth of a large limit cycle [larger red closed curve in (c) and (h), compare with turquoise curve in Fig. 10(h)]. In (d) and (i), the 3rd homoclinic bifurcation is illustrated, in which a small safe loop (magenta line) is formed by the manifolds of the saddle-node [compare with Fig. 10(j)]. This bifurcation leads to the disappearance of the small limit cycle and leaves only one attractor being the large limit cycle [red line in (e) and (j), compare with Fig. 10(l)].

this manifold has an even more complex shape; e.g., in (o), a part of this manifold should unwind from the vicinity of the unstable fixed point (empty circle in the upper part), but we cannot show this without overloading the figure. Also, this manifold extends well beyond the boundaries shown and has a similarly complex structure in the lower parts of panels in Figs. 11(k)–11(o), which we again do not show for the sake of clarity. Thus, the complexity of the shape of the stable manifold of the saddle-focus prevents us from illustrating this bifurcation in full.

With this, reorganization of the manifolds *away* from the homoclinic loop during this bifurcation would be qualitatively the same if the saddle-focus is replaced by a saddle node whose manifolds have a simpler shape and are easier to depict [see Figs. 11(f)–11(j)].

## E. Basins of attraction

In the context of optimization, our main interest is how homoclinic bifurcations amend the basins of attraction and lead to their merging. For a fictional two-dimensional system, Figs. 11(a)–11(e) show the basins of two coexisting attractors by different shades. Depiction of the basins is easy on the plane but difficult in higher-dimensional spaces; therefore, this figure can be used for a visual reference. Here, the yellow shade shows the basin of an attractor at or near an equivalent of  $x_2^{\min}$  (upper right part of the panel), whereas the basin of attractor at or near  $x_1^{\min}$  (lower left part of the panel) is not shaded.

By analogy with similar situations in ODEs, one can hypothesize that the stable manifold should make several turns around the three fixed points, thus making both basins of attraction stripy. Although we cannot verify this hypothesis by building stable manifolds of the DDE, we can numerically find the basins themselves and reveal the stable manifolds as their boundaries, as was done in Ref. 67 for a four-dimensional system.

The basin of attraction in (2) is a set of all initial functions  $\varphi(t)$ ,  $t \in [-\tau, 0]$ , such that all solutions starting from these functions converge to the given attractor. It is a subset of an infinite-dimensional phase space and difficult to visualize in full. However, we utilize an approach of Refs. 68 and 69 and consider only a subset of all possible initial conditions, namely, functions of a certain class parameterized by a finite number of parameters. In our case, we choose the simplest class of constant initial functions,  $\varphi(t) = x = \text{const}$ ,  $t \in [-\tau, 0]$ . Such functions can be directly compared with the positions of fixed points in (2).

Importantly, numerical simulations of (2) and (9), as well as of (2) with several similar potentials, including those specified in Secs. S-II and S-III of the [supplementary material](#), revealed that at positive  $\tau$  from some initial conditions, such systems systematically go to infinity. Thus, infinity represents an additional attractor with its own basin and boundaries, which could be revealed numerically.

The basins of attraction of (2) and (9) are given in Fig. 14 for a range of  $\tau$  in the vicinity of the 1st homoclinic bifurcation. The striking feature of this plot is the large basin of attraction of infinity (blue shade), which expands with growing  $\tau$ . Below the bifurcation point  $\tau = 1.53$ , in addition to infinity, there are two attractors

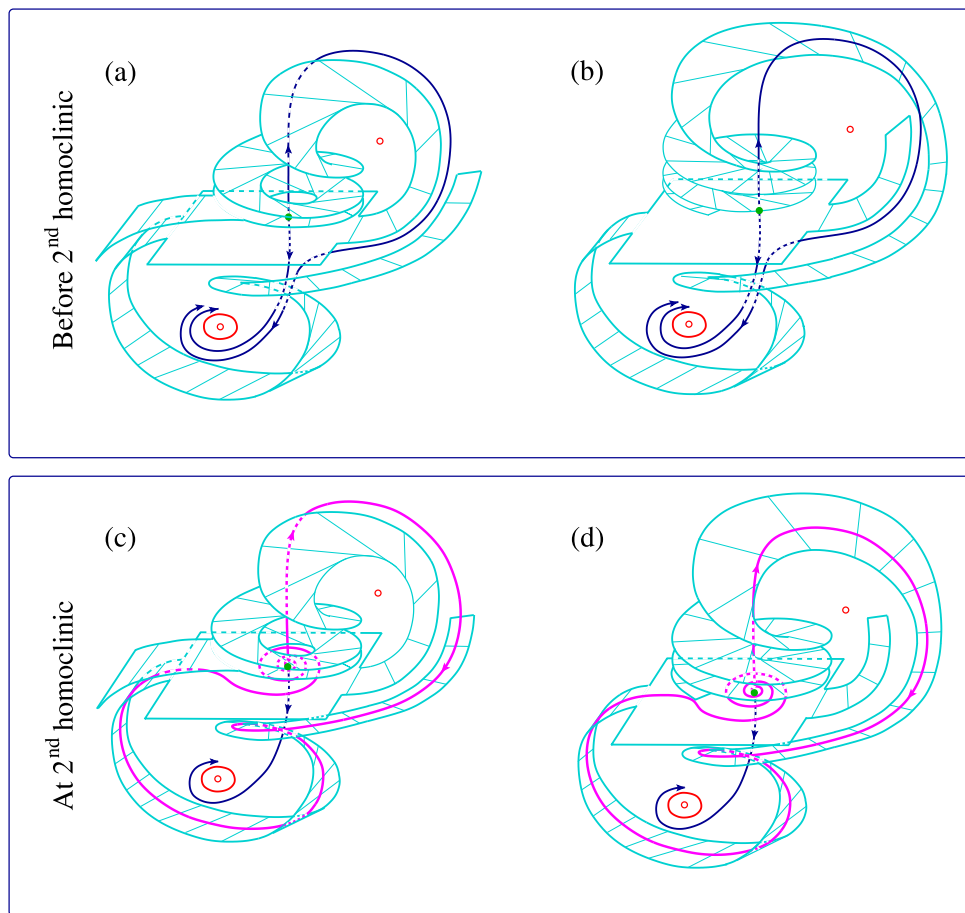


**FIG. 13.** Schematic illustration of the 2nd homoclinic bifurcation in (2) and (9) at  $\tau \approx 2.4307$ , which creates a large safe homoclinic loop of  $x^{\max}$  subsequently giving birth to a large attractor embracing all fixed points. (a) and (b) Before the bifurcation [compare with Figs. 10(e), 12(a), and 12(f)] and (c) and (d) at the bifurcation [compare with Figs. 10(f), 12(b), and 12(g)]. The cyan surface shows a stable manifold and the blue line shows an unstable manifold of the saddle-focus at  $x^{\max}$  (green filled circle). Unstable fixed points at  $x_{1,2}^{\min}$  are shown by empty red circles, and the limit cycle around  $x_1^{\min}$  is shown by a red line in the lower parts of the panels. A spiraling cyan surface in the upper part of each panel shows a portion of the stable manifold (a) and (c) not participating in the homoclinic bifurcation and (b) and (d) participating in the bifurcation. The homoclinic loop lies on the portion of the stable manifold shown in (d), which at the bifurcation point and close to  $x^{\max}$  has a shape of a closed helicoid with an infinite number of turns.

on different sides of  $x^{\max}$ , and on the plot, we do not distinguish between fixed points and limit cycles. Due to the 1st homoclinic bifurcation at  $\tau \approx 1.53$ , the basin of attractor at or near  $x_2^{\min}$  (red shade) collapses, and at  $1.53 < \tau < 2.43$  besides the infinity, there is only one attractor at or near  $x_1^{\min}$  (green shade).

Figure 14 reveals that the basins of attraction at least before the 1st homoclinic bifurcation are stripy and, therefore, confirms the hypothesis that the stable manifold of  $x^{\max}$  makes several turns around the three fixed points [compare with Figs. 11(b) and 11(c)].

## F. Second homoclinic bifurcation

As mentioned in Sec. IV B, the 2nd homoclinic bifurcation cannot be predicted based on the theorems overviewed in Sec. II B. The numerical simulations suggest that it consists of forming a

large homoclinic loop embracing all fixed points [magenta line in Fig. 10(f)] and results in the birth of a large limit cycle [turquoise line in Fig. 10(h)].

The formation of a large homoclinic loop involves a different pair of manifolds of the saddle-focus  $x^{\max}$ , as compared to those forming the 1st small loop. As before, given the difficulty of making clear and easily interpretable sketches of intricately shaped manifolds of a saddle-focus, we initially illustrate the respective homoclinic loop in a two- [Figs. 12(a)–12(c)] and three-dimensional [Fig. 12(f)–12(h)] fictional systems with saddle-nodes. Notations are the same as in Fig. 11, and in addition, brown lines in (b)–(e) show typical phase trajectories.

Figures 12(a)–12(c) explain how the basin of a newly born attractor (large cycle) is formed thanks to the rearrangement of manifolds. Specifically, in (a), the yellow shade shows the basin of

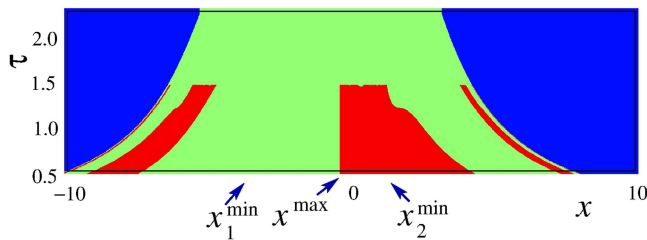


**FIG. 14.** Basins of attraction of (2) and (9) with safe homoclinic loops as a function of  $\tau$ . Different shades mark points  $x$  such that, from initial conditions  $\varphi(t) = x$ ,  $t \in [-\tau, 0]$ , the phase trajectory converges to the following attractors: infinity (blue), fixed point at, or limit cycle around,  $x_1^{\min}$  (green), fixed point at, or limit cycle around,  $x_2^{\min}$  (red). Above the 1st homoclinic bifurcation point  $\tau = 1.53$ , there is no local attractor at or near  $x_2^{\min}$ . Compare the stripy structure of the basins below  $\tau = 1.53$  here and in Figs. 11(a)–11(c).

the only attractor available just before the bifurcation, i.e., of the limit cycle around an equivalent of  $x_1^{\min}$  [red line, compare with Figs. 10(d) and 10(e)]. At the 2nd homoclinic bifurcation in (b), this basin becomes bounded. After the bifurcation in (c), the manifolds are rearranged to form the boundary of the new basin (non-shaded) of the large limit cycle born from the homoclinic loop (large red closed curve).

Figures 12(f)–12(h) demonstrate the same sequence of events, only in a three-dimensional system with a two-dimensional stable manifold of the saddle-node. This illustration is an intermediate stage before depicting manifolds of a saddle-focus in the three-dimensional space while they undergo a similar reorganization.

The respective manifolds of a saddle-focus of (2) and (9), in the center manifold reduction and in the vicinity of the large homoclinic loop, are sketched in Fig. 13. Panels (a) and (b) illustrate the situation just before the 2nd (large) homoclinic loop is formed [compare with Fig. 12(f)], and (c) and (d) illustrate the instant of this large loop formation [compare with Fig. 12(g)].

The picture of the manifolds here is even more complex than near the small homoclinic loop sketched in Fig. 11(n) because of the spiraling of the stable manifold as it approaches the saddle focus from *both* sides. However, away from the saddle focus, the stable manifold is qualitatively similar to the one of a saddle-node.

Before the homoclinic loop, the stable manifold, whose different segments are shown by cyan surfaces in panels (a) and (b) of Fig. 13, wraps itself around all the three fixed points more than once, thus making more than one layer similarly to the manifold shown in Fig. 12(a) by a dashed cyan line.

As a result, the one-dimensional unstable manifold of the saddle-focus [blue line in Figs. 13(a) and 13(b)] goes *between* the two layers of the stable manifold upward from  $x^{\max}$  and then toward the local attractor near  $x_1^{\min}$  (red line in the lower left parts of the panels), just like in Figs. 12(a) and 12(f). At the instant of the homoclinic bifurcation at  $\tau \approx 2.4307$ , a segment of the stable manifold collides with the saddle-focus and captures the unstable manifold, which now forms a large safe homoclinic loop [magenta line in Fig. 13(d), compare with Figs. 10(f) and 10(g) and 12(b) and 12(g)]. Note that at the instant of bifurcation, the helicoid-shaped portion of the stable

manifold *containing* the homoclinic loop [upper part of Fig. 13(d)] makes an infinite number of turns as it approaches the saddle focus.

As  $\tau$  grows, the loop disappears and gives birth to a large limit cycle embracing all three fixed points, which are similar to large red closed curves in Figs. 12(c) and 12(h). The respective large cycle of (2) and (9) is given by a turquoise line in Fig. 10(h).

### G. Third homoclinic bifurcation, chaos, and infinity

The 3rd homoclinic bifurcation takes place at  $\tau = 2.4499$  [see Fig. 8(b)] and eliminates the small limit cycle to the left of  $x^{\max}$ , i.e., around  $x_1^{\min}$ , as illustrated with phase portraits in Figs. 10(i)–10(l) and with sketches of a similar bifurcation in systems with a saddle-node in Figs. 12(c)–12(e) and 12(h)–12(j). This bifurcation is qualitatively the same as the 1st homoclinic. At  $\tau > 2.4499$ , there are no more local attractors in the system.

At  $\tau \in (2.4499, 3, 33]$ , the system has a single large attractor enclosing all fixed points. This attractor is initially a limit cycle of period one [Fig. 10(l)], but with increasing  $\tau$ , it undergoes a cascade of period-doubling bifurcations [Figs. 10(m) and 10(n)] and becomes chaotic [Fig. 10(o)]. Note that the phase trajectory on the chaotic attractor visits the close vicinities of all three fixed points, which is roughly similar to the effect caused by adding large random noise to (1) in simulated annealing.

As  $\tau$  exceeds 3.33, the chaotic attractor disappears and the trajectory goes to infinity [Fig. 10(p)]. We cannot specify the exact reason for this and can only hypothesize that the manifold bounding the basin of attraction of chaos appears involved in some global bifurcation. Since we cannot visualize this manifold, we cannot verify our hypothesis. However, our studies of a considerable number of systems of the form (2) with various multi-well landscapes  $V$  suggest the universality of this phenomenon.

Specifically, it seems that in such systems, as  $\tau$  becomes sufficiently large, a chaotic attractor enclosing all extrema of  $V$  is initially born (although it might turn into a periodic one at even larger  $\tau$ , e.g., when periodic windows in chaos appear<sup>70</sup>). However, when  $\tau$  is increased further, the large attractor is inevitably destroyed, and the trajectory escapes to infinity from all initial conditions.

It is important to appreciate that the infinity is present as some kind of an attractor at all values of  $\tau > 0$ . To make more specific predictions about encountering attractors at infinity, a rigorous investigation of the necessary and sufficient conditions for the existence of unbounded solutions in nonlinear systems of type (2) would be required.

### H. Different forms of homoclinics

We also studied the phenomena induced by the increase of  $\tau$  in a slightly different system of the form (2) with a double-well landscape  $V(x)$  specified by Eq. (S21) in the [supplementary material](#), in which at the instants of homoclinic bifurcations, the saddle focus was below AH bifurcations but had a positive saddle quantity. According to Shilnikov's theorem for ODEs,<sup>55,56</sup> in such cases, the homoclinic loops are expected to be dangerous, and their breakdown should lead to the formation of chaotic attractors. However, to the best of our knowledge, this result has not been verified for DDEs. Our numerical studies did not reveal any obvious differences between the sequence of bifurcations in the systems of the form (2)

with double-well landscapes  $V$  with dangerous or safe homoclinic loops, and the observed phenomena looked very similar when studied with the same numerical accuracy. Thus, whether the dangerous homoclinic loop gave birth to chaos or not, it did not affect the order of bifurcations, and the same key phenomena were observed.

In addition, Sec. S-II in the [supplementary material](#) presents a similar, albeit briefer, analysis of bifurcations in (2) with a two-well potential  $V$  for which at the instant of the 1st homoclinic bifurcation, the fixed point  $x^{\max}$  is past AH bifurcations. There, the homoclinic orbit is formed by the manifolds of the saddle cycle born from  $x^{\max}$ , which become tangent to each other, as described in Sec. II C. Nevertheless, the general sequence of bifurcations there is very similar to the one in (2) and (9).

## V. RELEVANCE TO OPTIMIZATION

In the context of optimization, the delay-induced bifurcations in (2) inform us about the mechanisms behind the removal of the barriers between the local minima of the two-well potential function, which could be potentially applicable to multi-well landscapes as well. Indeed, in the DDE (2), the barriers between the local minima of  $V$  are formed by the stable codimension-one manifolds of the saddle fixed point at the maximum of  $V$  or of the saddle cycle born from this point. These manifolds are the boundaries of the basins of attractors localized near the minima of  $V$ . Delay-induced homoclinic bifurcations do not make these fixed points of manifolds disappear but rearrange manifolds in such a way that they cease to separate different basins and hence to be the barriers.

The absence of barriers between the local minima and the birth of the large chaotic attractor enables the phase trajectory to visit the vicinities of all minima. Thus, the delay acts by a rough analogy with the random noise in a famous optimization technique of simulated annealing.<sup>38</sup>

One possible optimization procedure using the delay  $\tau$  as a control parameter is illustrated in Fig. 8(c). To obtain this figure, Eqs. (2) and (9) were solved as  $\tau$  was decreased from some positive value to zero. Specifically, at  $t = 0$ , the system was launched from initial conditions belonging to the large chaotic attractor at  $\tau = 3.3$ . Then,  $\tau$  was monotonously decreased in a step-wise manner from 3.3 to zero with small steps of the size 0.01. The duration of each step was 50 time units, during which the phase trajectory approached the attractor closest to the last state from the previous step. The decrease of  $\tau$  was almost adiabatic.

With this procedure, at  $\tau = 0$ , the system ended up at the minimum  $x_1^{\min}$ , at which the modulus of the Jacobian,  $|J|$ , is smaller than at  $x_2^{\min}$  [see Fig. 8(a)] and which, therefore, undergoes AH bifurcations at a larger value of  $\tau$  [see Fig. 8(b)]. This minimum  $x_1^{\min}$  is not only flatter than  $x_2^{\min}$ , but also broader due to which the local attractor around  $x_1^{\min}$  survives for larger values of  $\tau$  than the one around  $x_2^{\min}$ .

Under the adiabatic decrease of  $\tau$  within approximately [1.53, 3.3], i.e., above the 1st homoclinic, at every instantaneous value of  $\tau$ , the solution is close to the only attractor corresponding to this value of  $\tau$ . The latter is either the one embracing two minima at larger  $\tau$  or the one localized near, or at,  $x_1^{\min}$  at smaller  $\tau$ . When  $\tau$  decreases below the 1st homoclinic at  $\tau \approx 1.53$ , the local attractor around  $x_2^{\min}$  appears. However, the solution is not affected by this

event and remains in the vicinity of  $x_1^{\min}$  until  $\tau$  reaches zero. Since in this example  $x_1^{\min}$  happens to be the lowest minimum, an adiabatic decrease of  $\tau$  has demonstrated optimization as required.

In Sec. S-II B of the [supplementary material](#), optimization with an adiabatic decrease of  $\tau$  is demonstrated for a subtly different example of a system with a two-well potential, in which all homoclinic bifurcations take a different form as compared to the ones in (2) and (9). To summarize, an adiabatic decrease of  $\tau$  delivers the flattest and broadest minimum of the two.

It is clear that in a general two-well potential, such a minimum would not necessarily be the lowest one, and an adiabatic decrease of  $\tau$  would not result in optimization. To overcome this issue and to reduce the dependence on the shape of the potential, we can use the fact that larger delay induces chaotic, i.e., random-looking, behavior forcing the phase trajectory to visit the vicinities of all minima. Then, at some sufficiently large value of  $\tau$ , at some randomly chosen time  $t$ , the system can be found in one of these vicinities. If at this moment  $\tau$  starts to decrease relatively fast, i.e., in a non-adiabatic manner, the phase trajectory would fail to approach any attractor existing at any fixed value of  $\tau$ . This way, at  $\tau = 0$ , the system could end up in the same well it was before  $\tau$  started to decrease, and to whose bottom, it would then converge following standard gradient descent (1). Several repetitions of the same experiment with  $\tau$  being increased from, and then decreased to, zero would eventually reveal all available minima whose depths could be compared at the end, and the lowest one would be identified.

To illustrate this effect, consider (2) with a double-well  $V$  and the respective  $f = -V'$  specified as follows:

$$\begin{aligned} V(x) &= -2e^{-2(x-1)^2} - e^{-0.5(x+3)^2} + 0.01(x+1)^4, \\ f(x) &= -8e^{-2(x-1)^2}(x-1) - e^{-0.5(x+3)^2}(x+3) \\ &\quad - 0.04(x+1)^3. \end{aligned} \quad (10)$$

The functions  $V(x)$ ,  $f(x)$ , and  $J(x) = f'(x)$  are shown in Fig. 15(a) by blue, red, and green lines, respectively. Red/green circles indicate the positions of the fixed points at the potential minima/maximum. Here, the flattest and broadest minimum is  $x_1^{\min}$ , but the lowest minimum is  $x_2^{\min}$ .

First, we launch this system at  $t = 0$  from the initial conditions  $x(t) = 2$  for  $t \in [-2.1, 0]$  and  $\tau = 2.1$  and start to find the numerical solution  $x(t)$  while decreasing  $\tau$  at a relatively low rate. Specifically, after 0.1 time units,  $\tau$  is abruptly decreased to 2.0 and kept at this value for another 0.1 time units while the system is being solved. The process continues while  $\tau$  is being decreased in a step-wise manner to zero in steps of 0.1. The resultant solution  $x(t)$  is given in Fig. 15(b) by black symbols and demonstrates that with this relatively slow decrease of  $\tau$ , the system ends up near the flattest and broadest minimum  $x_1^{\min}$ .

Next, we repeat the process of decreasing  $\tau$  step-wise but make the duration of every step ten times smaller than above, i.e., 0.01. The resultant solution is shown in Fig. 15(b) by red symbols and demonstrates that the system ends up in the well of the lowest minimum  $x_2^{\min}$ . In Fig. 15(c), the same solutions are shown as in (b) but now against the current value of  $\tau$  for the convenience of comparison.



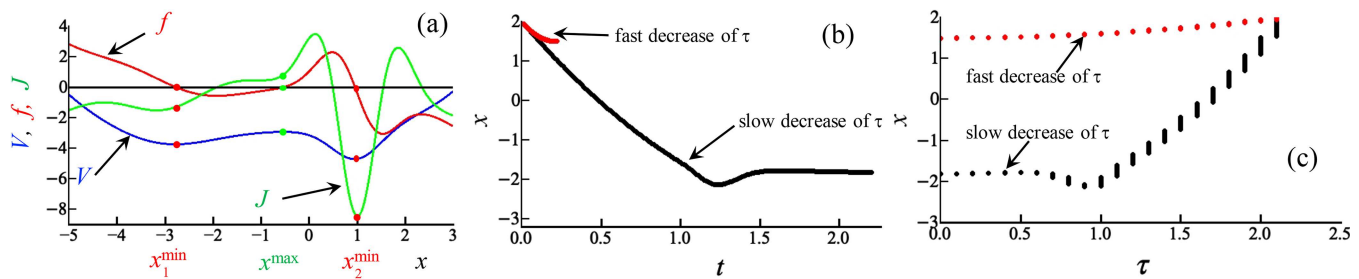


**FIG. 15.** Illustration of optimization by decreasing the delay in system (2) and (10) where the lowest minimum of  $V$  at  $x_2^{\min}$  is not the flattest or the broadest. Such lowest minimum can be delivered with a fast decrease of  $\tau$ . (a) Functions  $V(x)$  (blue line),  $f(x)$  (red line), and  $J(x) = f'(x)$  (green line) specified by (10). Red/green circles show positions of fixed points at the minima/maxima of  $V$ . (b) Solutions  $x(t)$  launched from  $x(t) = 2$  for  $t \in [-2.1, 0]$  for  $\tau$  decreasing in a step-wise manner from 2.1 to zero in steps of 0.1 of various duration: a slower decrease with step 0.1 (black points) and a faster decrease with step 0.01 (red points). (c) Points belonging to solutions  $x(t)$  shown against the current value of  $\tau$ , while it decreases as described in (b). Notations are as in (b).

Thus, the fast decrease of  $\tau$  delivers the lowest minimum, which is not the broadest or the flattest.

## VI. DISCUSSION AND CONCLUSION

The fact of the occurrence of homoclinic bifurcations induced by the increase of delay in (2) with a multi-well potential  $V$  could be predicted based on the theorems overviewed in Sec. II. However, the specific forms of these bifurcations, their dependence on the features of  $V$ , and their ordering do not follow from these theorems.

For a general nonlinear DDE with an arbitrary nonlinearity and an arbitrary dependence on delay, it is usually impossible to predict the delay-induced changes in the behavior before actually observing this behavior using numerical analysis. However, we hypothesized and verified that for a special class of scalar nonlinear models (2), in which the right-hand side depends only on the delayed variable and represents the negative of the gradient of a *two-well* potential, it is possible to make some qualitative predictions of the phenomena induced by the increase of the delay.

Specifically, we tested and confirmed our initial hypothesis that the increase of the delay  $\tau$  should lead to a chain of homoclinic bifurcations, leading to the disappearance of attractors localized around the minima of  $V$  and to the eventual birth of a large attractor embracing both local minima, which forces the system to visit the vicinity of every minimum, including the global minimum, as time goes by.

The latter resembles the effect from a random term within simulated annealing<sup>38</sup> but is achieved in a purely deterministic manner. It also has some similarity with quantum annealing assumed in quantum computers,<sup>71</sup> which is performed thanks to the ability of particles to tunnel the potential barriers between the local minima of energy function. In our case, thanks to the delay, the barrier between the two minima of the cost function disappears, thus enabling the system to freely wander between both minima. Indeed, the barrier between the minima is ultimately the manifold of the saddle fixed point at the maximum, which separates the basins of attractors localized near the minima. Although after the homoclinic bifurcation, neither this manifold nor the maximum disappears, the manifold stops being the barrier, and hence, the barrier ceases to exist.

Another important observation is that for the values of the delay exceeding some threshold, no attractors at finite locations survive in the system, and the phase trajectory tends to infinity from any initial conditions. This effect has been observed numerically for all examples considered; however, it would be useful to verify its validity analytically in the future work. In this context, it would be interesting to understand whether the death of the last attractor at a finite location is linked to reorganization of manifolds or is caused by other reasons. In the absence of numerical methods for visualizations of the relevant manifolds in DDEs, this matter cannot be resolved by their direct computation at this stage. With this, we are not aware of any relevant theoretical results, which could readily suggest a plausible explanation behind this phenomenon. Hopefully, this could be clarified with further development of numerical approaches and/or theory of bifurcations in DDEs.

Our results show that the realization of the particular forms of homoclinic bifurcations depends not only on the parameters of the potential wells and a hump, such as the depth, width, and sharpness, but also on the relationships between them. Specifically, the local attractor around one of the minima may collide either with the maximum itself or with the saddle cycle born from this maximum. Prior to the disappearance of the local attractor through a homoclinic bifurcation, bistability may either occur or fail to occur.

However, the exact nature of homoclinic bifurcations does not seem to change the general sequence of events as  $\tau$  grows, which has been confirmed also with a number of additional examples, including those provided in the [supplementary material](#). Thus, we are satisfied with our ability to qualitatively predict the events induced by the increase of time delay in a highly nonlinear system of a special form.

Our results are a pre-requisite to understanding and prediction of the phenomena in general nonlinear delay-differential equations, in which the nonlinear function in the right-hand side depends solely on the delayed variable. They will inform building delay systems with prescribed controllable properties in applications. For example, if one wishes to obtain a system demonstrating a desirable sequence of bifurcations with the increase of delay, one could use the knowledge obtained in order to design the landscape  $V$  of (2) with the necessary properties. Specifically, one could fine-tune the



relative depths, widths, and shapes of the individual wells and humps in  $V$  in order to ensure a certain order and forms of homoclinic bifurcations.

A considerable motivation for this study has been the idea of Ref. 41 to use delay-induced bifurcations for optimization. Here, we demonstrated how optimization could be achieved for some two-well cost functions if one uses the delay as the only control parameter. Further studies will be needed to explore the possibility to extend this approach to cost functions depending on many variables.

## SUPPLEMENTARY MATERIAL

See the [supplementary material](#) that contains an overview of the analysis of local dynamics of DDEs around the fixed points (Sec. S-I), considers an example of a delay system (2) with a double-well potential slightly different from that specified by (9), where a similar, but subtly different, chain of homoclinic bifurcations is observed (Sec. S-II), and gives three additional examples of double-well potential functions resulting in a similar chain of bifurcations as in examples considered in the paper (Sec. S-III).

## AUTHORS' CONTRIBUTIONS

N.B.J. proposed and designed the research, did all numerical simulations described in the paper except for Fig. 14, interpreted the results, and wrote the paper. C.J.M. performed an analytical treatment of a delay-differential equation in Sec. III and in the [supplementary material](#); did preliminary numerical simulations of a system not illustrated in the paper, which delivered rough initial results; calculated basins of attraction for Fig. 14; and edited the paper. Both authors contributed to the discussions.

## ACKNOWLEDGMENTS

The authors are grateful to Dmitri Tseluiko for helpful discussions about Shilnikov's theorem and for help in preparing Figs. 11(k)–11(o) and to Alexander Balanov for helpful discussions and feedback on the draft of this manuscript. C.J.M. was supported by the Engineering and Physical Sciences Research Council (UK) [EPSRC(GB)] during his Ph.D. studies in Loughborough University (Grant No. EP/P504236/1).

## DATA AVAILABILITY

Data sharing is not applicable to this article as no new data were created or analyzed in this study.

## REFERENCES

- G. E. Hutchinson, "Circular casual systems in ecology," *Ann. N. Y. Acad. Sci.* **50**, 221–246 (1948).
- W. J. Cunningham, "A nonlinear differential-difference equation of growth," *Proc. Natl. Acad. Sci. U.S.A.* **40**, 708–713 (1954).
- M. C. Mackey and L. Glass, "Oscillation and chaos in physiological control systems," *Science* **197**, 287–289 (1977).
- G. A. Bocharov and A. A. Romanyukha, "Mathematical model of antiviral immune response. III. Influenza A virus infection," *J. Theor. Biol.* **167**, 323–360 (1994).
- K. L. Cooke and P. van den Driessche, "Analysis of an SEIRS epidemic model with two delays," *J. Math. Biol.* **35**, 240–260 (1996).
- G. S. K. Wolkowicz and H. X. Xia, "Global asymptotic behavior of a chemostat model with discrete delays," *SIAM J. Appl. Math.* **57**, 1019–1043 (1997).
- R. V. Culshaw and S. Ruan, "A delay-differential equation model of HIV infection of CD4(+) T-cells," *Math. Biosci.* **165**, 27–39 (2000).
- P. Smolen, D. A. Baxter, and J. H. Byrne, "Modeling circadian oscillations with interlocking positive and negative feedback loops," *J. Neurosci.* **21**, 6644–6656 (2001).
- P. W. Nelson and A. S. Perelson, "Mathematical analysis of delay differential equation models of HIV-1 infection," *Math. Biosci.* **179**, 73–94 (2002).
- M. Ursino and E. Magosso, "Role of short-term cardiovascular regulation in heart period variability: A modeling study," *Am. J. Physiol. Heart Circ. Physiol.* **284**, H1479–H1493 (2003).
- M. Villasana and A. Radunskaya, "A delay differential equation model for tumor growth," *J. Math. Biol.* **47**, 270–294 (2003).
- M. Dhamala, V. K. Jirsa, and M. Z. Ding, "Enhancement of neural synchrony by time delay," *Phys. Rev. Lett.* **92**, 074104 (2004).
- S.-N. Chow and J. Mallet-Paret, "Singularly perturbed delay-differential equations," in *Coupled Nonlinear Oscillators, Proceedings of the Joint U.S. Army-Center for Nonlinear Studies Workshop, Los Alamos, North-Holland Mathematics Studies*, Vol. 80, edited by J. Chandra and A. C. Scott (North-Holland, 1983), pp. 7–12.
- J. Mallet-Paret and R. D. Nussbaum, "Global continuation and asymptotic behaviour for periodic solutions of a differential-delay equation," *Ann. Mat. Pura Appl.* **145**, 33–128 (1986).
- S.-N. Chow, X.-B. Lin, and J. Mallet-Paret, "Transition layers for singularly perturbed delay differential equations with monotone nonlinearities," *J. Dyn. Differ. Equ.* **1**, 3–43 (1989).
- R. M. Goodwin, "The nonlinear accelerator and the persistence of business cycles," *Econometrica* **19**, 1–17 (1951).
- U. an der Heiden and H.-O. Walther, "Existence of chaos in control systems with delayed feedback," *J. Differ. Equ.* **47**, 273–295 (1983).
- V. L. Arnold, *Geometrical Methods in the Theory of Ordinary Differential Equations*, 2nd ed. (Springer-Verlag, 1988).
- J. Guckenheimer and P. Holmes, *Nonlinear Oscillations, Dynamical Systems, and Bifurcations of Vector Fields* (Springer-Verlag, 1997), Vol. 42.
- Y. A. Kuznetsov, *Elements of Applied Bifurcation Theory* (Springer-Verlag, 1998), Vol. 112.
- L. P. Shilnikov, A. L. Shilnikov, D. V. Turaev, and L. O. Chua, *Methods of Qualitative Theory in Nonlinear Dynamics, Part 2* (World Scientific Publishing Co., Inc., 2001), Vol. 5.
- S.-N. Chow, "Existence of periodic solutions of autonomous functional differential equations," *J. Differ. Equ.* **15**, 350–378 (1974).
- J. L. Kaplan and J. A. Yorke, "On the nonlinear differential delay equation  $x'(t) = -f(x(t), x(t-1))$ ," *J. Differ. Equ.* **23**, 293–314 (1977).
- J. Wei, "Bifurcation analysis in a scalar delay differential equation," *Nonlinearity* **20**, 2483 (2007).
- C. Huang, Z. Yang, T. Yi, and X. Zou, "On the basins of attraction for a class of delay differential equations with non-monotone bistable nonlinearities," *J. Differ. Equ.* **256**, 2101–2114 (2014).
- J. K. Hale and X.-B. Lin, "Heteroclinic orbits for retarded functional differential equations," *J. Differ. Equ.* **65**, 175–202 (1986).
- K. Green, B. Krauskopf, and K. Engelborghs, "Bistability and torus break-up in a semiconductor laser with phase-conjugate feedback," *Physica D* **173**, 114–129 (2002).
- T. Sahai and A. Vladimirovsky, "Numerical methods for approximating invariant manifolds of delayed systems," *SIAM J. Appl. Dyn. Syst.* **8**, 1116–1135 (2009).
- C. M. Groothedde and J. D. Mireles James, "Parameterization method for unstable manifolds of delay differential equations," *J. Comput. Dyn.* **4**, 21–70 (2017).
- J. Y. Gao and L. M. Narducci, "The effect of modulation in a bistable system with delay," *Opt. Commun.* **58**, 360–364 (1986).
- K. Green and B. Krauskopf, "Global bifurcations and bistability at the locking boundaries of a semiconductor laser with phase-conjugate feedback," *Phys. Rev. E* **66**, 016220 (2002).

- <sup>32</sup>B. F. Redmond, V. G. LeBlanc, and A. Longtin, "Bifurcation analysis of a class of first-order nonlinear delay-differential equations with reflectional symmetry," *Physica D* **166**, 131–146 (2002).
- <sup>33</sup>C. Quinn, J. Sieber, A. S. von der Heydt, and T. M. Lenton, "The mid-pleistocene transition induced by delayed feedback and bistability," *Dyn. Stat. Clim. Syst.* **3**, 1–17 (2018); available at <https://academic.oup.com/climatesystem/article/3/1/dzy005/5089151>.
- <sup>34</sup>M. W. Hirsch, S. Smale, and R. L. Devaney, *Differential Equations, Dynamical Systems, and an Introduction to Chaos* (Academic Press, Boston, MA, 2004).
- <sup>35</sup>R. Horst and P. M. Pardalos, *Handbook of Global Optimization* (Springer, 1995).
- <sup>36</sup>P. M. Pardalos and H. E. Romeijn, *Handbook of Global Optimization* (Kluwer Academic Publishers, 2002), Vol. 2.
- <sup>37</sup>H. Kushner and D. Clark, *Stochastic Approximation Methods for Constrained and Unconstrained Systems*, Applied Mathematical Science Series 26 (Springer, 1978).
- <sup>38</sup>S. Kirkpatrick, C. D. Gelatt, Jr., and M. P. Vecchi, "Optimization by simulated annealing," *Science* **220**, 671–680 (1983).
- <sup>39</sup>F. Aluffi-Pentini, V. Parisi, and F. Zirilli, "Global optimization and stochastic differential equations," *J. Optim. Theor. Appl.* **47**, 1–16 (1985).
- <sup>40</sup>S. B. Gelfand and S. K. Mitter, "Recursive stochastic algorithms for global optimization in  $\mathbb{R}^d$ ," *SIAM J. Control Optim.* **29**, 999 (1991).
- <sup>41</sup>N. B. Janson and C. J. Marsden, "Optimization by delay," [arXiv:1902.08196](https://arxiv.org/abs/1902.08196) (2019).
- <sup>42</sup>R. D. Nussbaum, "Periodic solutions of some nonlinear, autonomous functional differential equations. II," *J. Differ. Equ.* **14**, 360–394 (1973).
- <sup>43</sup>R. D. Nussbaum, "Periodic solutions of some nonlinear autonomous functional differential equations," *Ann. Mat. Pura Appl.* **101**, 263–306 (1974).
- <sup>44</sup>J. L. Kaplan and J. A. Yorke, "Ordinary differential equations which yield periodic solutions of differential delay equations," *J. Math. Anal. Appl.* **48**, 317–324 (1974).
- <sup>45</sup>J. L. Kaplan and J. A. Yorke, "On the stability of a periodic solution of a differential delay equation," *SIAM J. Math. Anal.* **6**, 268–282 (1975).
- <sup>46</sup>J. Mallet-Paret, "Negatively invariant sets of compact maps and an extension of a theorem of Cartwright," *J. Differ. Equ.* **22**, 331–348 (1976).
- <sup>47</sup>R. D. Nussbaum, "Global bifurcation of periodic solutions of some autonomous functional differential equations," *J. Math. Anal. Appl.* **55**, 699–725 (1976).
- <sup>48</sup>S.-N. Chow and B. Deng, "Bifurcation of a unique stable periodic orbit from a homoclinic orbit in infinite-dimensional systems," *Trans. Am. Math. Soc.* **312**, 539 (1989).
- <sup>49</sup>H.-O. Walther, "Homoclinic solution and chaos in  $x'(t)=f(x(t-1))$ ," *Nonlinear Anal. Theor. Methods Appl.* **5**, 775–788 (1981).
- <sup>50</sup>H.-O. Walther, "Bifurcation from a heteroclinic solution in differential delay equations," *Trans. Am. Math. Soc.* **290**, 213–233 (1985).
- <sup>51</sup>A. A. Andronov, E. A. Leontovich, I. I. Gordon, and A. G. Maier, *Theory of Bifurcations of Dynamic Systems on a Plane* (The Israel Program for Scientific Translations, 1971) (translated from Russian).
- <sup>52</sup>H.-O. Walther, "Homoclinic and periodic solutions of scalar differential delay equations," *Dyn. Syst. Ergod. Theory* **23**, 243–263 (1989).
- <sup>53</sup>H.-O. Walther, *Bifurcation from a Saddle Connection in Functional Differential Equations: An Approach with Inclination Lemmas* (Instytut Matematyczny Polskiej Akademii Nauk, 1990).
- <sup>54</sup>In ODEs, a homoclinic solution would be called doubly asymptotic to the fixed point (here,  $x = 0$ ), which means that it approaches this point when  $t$  tends not only to positive, but also to negative, infinity, given that time can be reversed. However, in DDEs, time cannot be generally reversed; therefore, the term *doubly asymptotic* might not be fully appropriate here.
- <sup>55</sup>L. P. Shilnikov, "A case of the existence of a denumerable set of periodic motions," *Dokl. Akad. Nauk SSSR* **160**, 558–561 (1965); available at [http://www.mathnet.ru/php/archive.phtml?wshow=paper&jrnid=dan&papid=30608&option\\_lang=eng](http://www.mathnet.ru/php/archive.phtml?wshow=paper&jrnid=dan&papid=30608&option_lang=eng).
- <sup>56</sup>L. P. Shilnikov, "On the generation of a periodic motion from trajectories doubly asymptotic to an equilibrium state of saddle type," *Math. USSR-Sb.* **6**, 427 (1968).
- <sup>57</sup>N. Gavrilov and L. Shilnikov, "On three-dimensional systems close to systems with a structurally unstable homoclinic curve: I," *Math. USSR-Sb.* **17**, 467–485 (1972).
- <sup>58</sup>N. Gavrilov and L. Shilnikov, "On three-dimensional systems close to systems with a structurally unstable homoclinic curve: II," *Math. USSR-Sb.* **19**, 139–156 (1973).
- <sup>59</sup>J. K. Hale and X.-B. Lin, "Examples of transverse homoclinic orbits in delay equations," *Nonlinear Anal. Theor. Methods Appl.* **10**, 693–709 (1986).
- <sup>60</sup>B. Krauskopf and H. Osinga, "Two-dimensional global manifolds of vector fields," *Chaos* **9**, 768–774 (1999).
- <sup>61</sup>R. Castelli, J.-P. Lessard, and J. D. Mireles James, "Parameterization of invariant manifolds for periodic orbits I: Efficient numerics via the Floquet normal form," *SIAM J. Appl. Dyn. Syst.* **14**, 132–167 (2015).
- <sup>62</sup>B. Krauskopf and K. Green, "Computing unstable manifolds of periodic orbits in delay differential equations," *J. Comput. Phys.* **186**, 230–249 (2003).
- <sup>63</sup>J. K. Hale and S. M. Verduyn Lunel, *Introduction to Functional Differential Equations* (Springer, 1993), Vol. 99.
- <sup>64</sup>P. Aguirre, B. Krauskopf, and H. Osinga, "Global invariant manifolds near homoclinic orbits to a real saddle: (Non)orientability and flip bifurcation," *SIAM J. Appl. Dyn. Syst.* **12**, 1803–1846 (2013).
- <sup>65</sup>P. Aguirre, B. Krauskopf, and H. M. Osinga, "Global invariant manifolds near a Shilnikov homoclinic bifurcation," *J. Comput. Dyn.* **1**, 1–38 (2014).
- <sup>66</sup>J. Carr, "The application of centre manifolds to amplitude expansions. I. Ordinary differential equations," *J. Differ. Equ.* **50**, 260–279 (1983).
- <sup>67</sup>A. G. Balanov, N. B. Janson, V. V. Astakhov, and P. V. E. McClintock, "Role of saddle tori in the mutual synchronization of periodic oscillations," *Phys. Rev. E* **72**, 026214 (2005).
- <sup>68</sup>J. Losson, M. C. Mackey, and A. Longtin, "Solution multistability in first-order nonlinear differential delay equations," *Chaos* **3**, 167–176 (1993).
- <sup>69</sup>S. R. Taylor and S. A. Campbell, "Approximating chaotic saddles for delay differential equations," *Phys. Rev. E* **75**, 046215 (2007).
- <sup>70</sup>S. H. Strogatz, *Nonlinear Dynamics and Chaos: With Applications to Physics, Biology, Chemistry, and Engineering* (Westview Press, Perseus, New York, 1994).
- <sup>71</sup>J. King, S. Yarkoni, J. Raymond, I. Ozfidan, A. D. King, M. Mohammadi Nevisi, J. P. Hilton, and C. C. McGeoch, "Quantum annealing amid local ruggedness and global frustration," D-Wave Technical Report Series No. 14-1003A-C, 2017.